

Lead Oxide (PbO) for direct conversion fluoroscopic detectors

By

OLEKSII SEMENIUK

Master of Science in Physics

Lakehead University

Thunder Bay, Ontario

2012

Lead Oxide (PbO) for direct conversion fluoroscopic detectors

Master of Science, 2011

Oleksii Semeniuk

Department of Physics

Lakehead University

Abstract

Polycrystalline Lead Oxide (PbO) is being investigated as a photoconductive materials for application as X-ray-to-charge transducer in direct conversion x-ray detectors used in fluoroscopy and radiology. Previous usage of PbO films in Plumbicon vacuum tubes for optical imaging ensures its appropriate photoconductive properties. In combination with high X-ray absorption coefficient due to high atomic number of Pb and the theoretically established conversion gain together indicates high potential for radiological medical imaging application.

Although very promising, at the current stage of development of PbO photoconductive layers thick enough for X-ray imaging applications have not yet achieved the expected conversion efficiency and not yet shown adequate temporal behavior for fluoroscopic applications: PbO suffers from image "lag" (i.e. the residual current following an x-ray pulse) and high dark current that limits the application of electric fields to below $3.5 \text{ V}/\mu\text{m}$, which is a major factor preventing the attainment of high conversion efficiency.

Here we present our study on optimization of PbO technology to produce thick uniform layers capable of withstanding elevated electric fields with extremely low dark current previously achievable only in optical grade thin PbO films used in Plumbicons. Application of high electric field and low dark current allowed us to measure the

electron-hole pair formation energy $W_{+/-}$ using the pulse height spectroscopy (PHS) method. Previous measurements of $W_{+/-}$ have been relatively indirect, whereas PHS is shown to be a more accurate technique. Fast temporal response for short X-ray pulses reveals high carrier mobility. Field dependency of $W_{+/-}$ (which is found to be higher than previously shown and to decrease as a function of electric field), dark current kinetics and X-ray response are reported. Our findings indicate that improved PbO layers are suitable for applications in direct conversion X-ray imaging detectors for a variety of applications.

Acknowledgements

I would like to thank my supervisor Dr. Alla Reznik from the Physics Department of Lakehead University for supporting and training me over the past two years. Her encouragement and guidance during the pursuit of my Masters degree gave hope to continue my research and cheered me up. I also want to thank my supervisory committee members, Dr. Guatam Das and Dr. Apichart Linhananta, for their kind guidance and directions. Their valuable advises during committee meetings helped me to acquire good knowledge and correct way of thinking.

I would also like to express my gratitude to Dr. John Rowlands, Dr. Julia Berashevich, Giovanni DeCrescenzo and Sergey Reznik for their help with the experiments and processing of data. Their discussions on lead oxide were very interesting and useful. I would like to extend my appreciation to Dr. M. Simon for his recommendations on PbO film growing techniques.

Table of Contents

Abstract.....	ii
Acknowledgements.....	iv
Table of content	v
List of figures.....	viii
List of acronyms	x
1 Chapter1: Introduction.....	1
1.1 A brief history of X-ray imaging	1
1.2 Overview of imaging systems.....	5
1.3 Analysis of modern X-ray to charge conversion techniques	8
1.3.1 Indirect conversion detection.....	8
1.3.2 Direct conversion detection	12
1.3.3 X-ray Light Valve.....	14
1.4 Attenuation of an X-ray beam by a medium.....	16
1.5 Physics behind the radiation detection techniques: types of interaction of radiation with matter	18
1.5.1 Photoelectric effect	18
1.5.2 Compton (incoherent) scattering.....	22
1.5.3 Rayleigh (coherent) scattering	25
1.6 PbO for direct conversion detectors	28
2 Chapter 2: Fabrication process and morphological analysis of PbO	30
2.1 Background of PbO deposition	30
2.2 Preparation of PbO layers	35
2.3 The Raman spectroscopy analysis of the grown layers	37
2.3.1 Introduction.....	37
2.3.2 Results.....	40

2.3.3	Discussion of PbO Raman spectrum.....	41
2.4	Conclusion	42
3	Chapter 3: PbO X-ray detector for fluoroscopic application	43
3.1	Introduction.....	43
3.2	Background: fundamentals of Plumbicon operation.....	44
3.3	Methods and materials	45
3.3.1	PbO with metal electrodes	45
3.3.2	Electronical model of experimental apparatus.....	46
3.4	X-ray response	52
3.4.1	Experimental apparatus.....	52
3.4.2	Results.....	49
3.4.3	Discussion.....	52
3.4.4	Conclusion	53
3.5	Measurement of X-ray photogeneration in polycrystalline PbO	53
3.5.1	X-ray induced photocurrent method	54
3.5.1.1	Experimental apparatus for X-ray photocurrent methods.....	54
3.5.1.2	Results.....	55
3.5.1.3	Discussion.....	57
3.5.2	The Pulsed Height Spectroscopy method	58
3.5.2.1	Experimental apparatus to measure PHS	59
3.5.2.2	Results.....	61
3.5.2.3	Discussion: PHS noise analysis	63
3.5.2.3.1	Quantum noise of PbO.....	64
3.5.2.3.2	Signal pile-up	65
3.5.2.3.3	Electronic Noise from preamplifier	65
3.5.2.3.4	Shot noise.....	76
3.5.2.3.5	Ballistic deficit	76
3.5.2.4	Conclusion	69
3.5.3	Dark current kinetics.....	70
3.5.3.1	Analysis of the dark current decay.....	70
3.5.3.2	Results and discussion	76

3.5.3.3 Conclusion	78
4 Chapter 4: Future work	79
4.1 Summary of the thesis	79
4.2 PbO blocking structure	80
Bibliography	83

List of Figures

Figure 1.1: The image quality versus the dose received by the patient	3
Figure 1.2: Scheme of a double emulsion film	6
Figure 1.3: Principle of operation of XRII.....	7
Figure 1.4: Scheme of active matrix imager	7
Figure 1.5: Indirect conversion detection scheme	9
Figure 1.6: The operational principal of the scintillator crystal.....	10
Figure 1.7: The dependence of resolution on scintillator thickness.....	11
Figure 1.8: Direct conversion detection scheme.....	13
Figure 1.9: Resolution vs. thickness of a photoconductor	13
Figure 1.10: Principle of operation of XLV	15
Figure 1.11: Attenuation of X-ray beam by matter.....	17
Figure 1.12: Photoelectric effect.....	19
Figure 1.13: Mass attenuation coefficient for several materials versus X-ray energy.....	21
Figure 1.14: Compton scattering.....	22
Figure 1.15: The Compton scatter distribution probability as a function of a deflection angle.....	24
Figure 1.16: Coherent scattering.....	25
Figure 1.17: Deflection probability of Rayleigh scattering versus scatter angle	26
Figure 1.18: The dependence of linear attenuation coefficient on X-ray energy for different detectors	28
Figure 2.1: Optical and SEM pictures of PbO	31
Figure 2.2: SEM pictures of PbO for different substrate temperatures	32
Figure 2.3: SEM scan of PbO cross-section	33
Figure 2.4: Effect of degradation on PbO	34
Figure 2.5: Schematic of PbO evaporator.....	36
Figure 2.6: Tetragonal α -PbO	38
Figure 2.7: Orthorhombic β -PbO	39
Figure 2.8: Lead Oxide Pb ₃ O ₄	40
Figure 2.9 Raman spectrum of grown PbO film	41

Figure 3.1: Plumbicon video tube	44
Figure 3.2: PbO with metal electrodes.....	45
Figure 3.3: Electrical model of experimental apparatus	46
Figure 3.4: X-ray response apparatus	49
Figure 3.5: Comparison of X-ray response waveform of PbO, a-Se and Si.....	50
Figure 3.6: X-ray response of lead oxide for different fields	51
Figure 3.7: X-ray of PbO for different temperatures	51
Figure 3.8: Set-up scheme for measurement of the X-ray induced current in PbO.....	55
Figure 3.9: Response of PbO on different X-ray pulse duration	56
Figure 3.10: Values of W_{\pm} obtained with X-ray induced current method.....	57
Figure 3.11: PHS apparatus	59
Figure 3.12: Response of PbO on 70 ns X-ray pulse.....	60
Figure 3.13: The pulsed height spectrum of PbO	62
Figure 3.14: Dependence of spectral mean on electric field.....	62
Figure 3.15: Values of W_{\pm} obtained with PHS method.....	63
Figure 3.16: Variation of spectral mean as a function of time.....	67
Figure 3.17: Noise of the system as a function of time	69
Figure 3.18: Dark current for PbO electrode structure and electron beam readout.....	71
Figure 3.19: Charge collection of the depletion region	74
Figure 3.20: ITO/PbO/Au energy diagram	76
Figure 3.21: Modification of the Au/PbO barrier	77
Figure 3.22: Dark current decay for different temperatures	77
Figure 4.1: PbO blocking structure.....	81

List of Acronyms

ALARA	As low as reasonably achievable
AMFPI	Active matrix flat panel imager
CCD	Charge coupled device
CMOS	Complementary metal oxide semiconductor
CsI	Cesium iodide
CT	X-ray Computed Tomography
CVD	Chemical vapor deposition
EHP	Electron-hole-Pair
FWHM	Full Width Half Maximum
ITO	Indium Tin Oxide
LAD	Laser assisted deposition
LC	Liquid crystal
MRI	Magnetic Resonance Imaging
OCT	Optical Coherent Tomography
PbO	Lead oxide
PET	Positron Emission Tomography
RF	Radio frequency
SEM	Scanning electron microscope
SNR	Signal to Noise Ratio
TFT	Thin Film Transistor
TOF	Time of flight
XRII	X-ray image intensifier
XLV	X-ray light valve
ZnCdS	Zinc cadmium sulfide

Chapter 1: Introduction

There is a long history of development in medical imaging, over which a number of different modalities were challenging each other in order to improve visualization of anatomical structural images of the human body. Although there are a number of different techniques currently available on the market X-ray imaging remains a key technique for diagnostic and interventional imaging procedures because it uniquely able to simultaneously permit high temporal and spatial resolution. From the beginning X-ray imaging has been split into two general approaches: radiology- a static “snap-shot” of the internal structures and fluoroscopy – a technique that allows visualization of real-time dynamic image sequences. The operation principle of all X-ray modalities is based on the variation of transmission of X-rays through the body, which is the result of different attenuation of human structures: bones attenuate X-rays more than soft tissue. This chapter is devoted to the history and the principle of operation of X-ray imaging techniques and follows the history of their improvements from the first fluorescent screen systems up to state-of-the art flat panel digital imaging devices. Recognition of the advantages and disadvantages of the currently available radiation detectors as well as a clear understanding of the requirements of medical imaging will provide essential guidance for further improvement of modern detectors. The aim of our study is to develop a technology that would permit reduction of the radiation exposure to the patient and medical personnel in radiology and fluoroscopy while maintaining the image quality.

1.1: A brief history of X-ray imaging

The day of November 8, 1895 when a German physicist Wilhelm Conrad Roentgen discovered X-rays can also be called a birth of X-ray imaging. Several other discoveries happened almost at the same time: discovery of radioactivity by Henry Becquerel in 1896 and of radium by Marie and Pierre Curie in 1898. All of them were honored by the Nobel Prize in Physics for their outstanding contribution to science. [1, 3]

Shortly after the discovery of X-rays, it became possible to make images of internal human anatomy. Both, X-ray and radium sources were used to produce radiographic

images or radiograms by shining X-rays through the body onto photographic plates. The use of X-rays for diagnostic imaging rapidly gained acceptance because radiograms could be obtained faster and had better contrast in comparison to those provided by radium or other radioactive sources available at that time. [3]

Soon after the discovery of X-rays it became possible to obtain X-ray images of a patient in real time. This procedure was called fluoroscopy. The first fluoroscope - a machine that permits obtaining anatomic structure images on the fly, consisted of an X-ray tube and a fluoroscopic screen between which the patient was located. The rear of the screen where image appears is covered by lead glass plate for two reasons: it allowed a radiologist to see the fluorescent light from the screen and at the same time it was protecting them from the X-rays that were not absorbed by the fluoroscopic phosphor screen [1].

The phosphor material used in these direct viewing fluorescent screens was Zinc Cadmium Sulfide (ZnCdS). When irradiated with X-rays the fluorescent screen produced visible light within a green-yellow spectrum which was however 30,000 times fainter than the light reflected from a piece of paper on sunny day. In order to get an eyes' peak sensitivity to green-yellow wavelengths, the dim fluoroscopic images were viewed in a darkened room and the fluoroscopists, at first, had to keep their eyes in complete darkness for a half an hour or more prior to fluoroscopy. The dark adaptation procedure was very time consuming, as it had to be repeated after every exposure to ambient light level. Red goggles were found to permit maintenance of dark adaptation. An improvement of image visualization was possible in the 1950s' with the invention of the X-ray image intensifier (XRII). These devices raised the brightness of the faint fluorescent image to the level necessary for full functioning of the human eye [1, 3]. There is a wide variety of X-ray image intensifiers. Although they have different design depending on application, but developed to serve the same goals: absorb X-rays emerging from the human body, and convert them into visible light. Nowadays, there are many digital and non-digital read out devices that provide high image quality, but none has reached perfection suggesting that more inventions are yet to come.

In parallel with development of X-ray imaging many other medical imaging modalities were invented. The development of tomography was the next level in revolutionizing imaging of human anatomy. Tomography is an imaging modality that allows one to see the internal body structure in sections or slices. When a set of images is obtained at different angles around the patient they undergo a special mathematical processing called a tomographic reconstruction. This development sets the stage for many tomographic modalities including Computer Tomography (CT), Positron Emission Tomography (PET), Single photon Emission Computed Tomography, Magnetic Resonance Imaging (MRI). All listed procedures have an advantage of tomographic imaging: they offer an opportunity to see the patients' anatomy slice by slice. Also, tomographic images taken at different viewing angles allow one to look at the object in real three dimensional mode [4]. However, conventional X-ray procedures (radiology and fluoroscopy) give a planar image of the human body and they still remain key and most frequently used (more than 50% of the market) modalities in diagnostic imaging.

Despite all the advantages of X-ray for medical imaging there are serious downsides related to harmful effect of ionizing radiation on the human body. Therefore, balancing between benefit and harm of X-rays implies an inherent tradeoff between image quality and an exposure to the patient, as it is depicted in figure below (Figure 1.1).

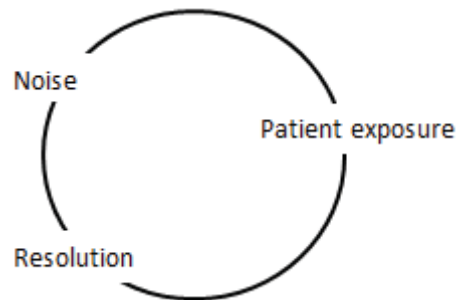


Figure 1.1: Tradeoff between the image quality and the dose received by the patient undergoing the X-Ray procedure [3].

In order to reduce the harm to the body, the dose of X-rays during the procedure should be reduced. However, at low doses of radiation system noise becomes more apparent and it degrades the image quality which could lead to misdiagnosis. On the other hand, in order to obtain an adequate image a higher dose of radiation must be

applied, but this causes more harm to the patient. So, there is a dilemma: we cannot sacrifice the image quality and we do not want to misdiagnose the patient. Within these constraints, the exposure to the patient is governed by the ALARA principle, which says that exposure has to be “As Low As Reasonably Achievable”. The dose should be established in such a way that even though ionizing radiation has negative effects on the patient, it must yield us more benefit than harm. Unfortunately, there is no flawless medical imaging modality in the modern world. In the Table 1.1 we have listed the advantages and disadvantages of the most widely used imaging techniques.

Table 1.1. Summary of advantages and disadvantages of most widely used imaging modalities.

Technique	Advantages	Disadvantages
Fluoroscopy	<ul style="list-style-type: none"> ○ Real time imaging ○ Provides dynamic and functional information ○ Inexpensive 	<ul style="list-style-type: none"> ● High total accumulated dose ● 2-D imaging ● Poor soft tissue contrast
Ultrasound	<ul style="list-style-type: none"> ○ Not harmful in diagnostic applications ○ Real time imaging ○ Tomographic 	<ul style="list-style-type: none"> ● Operator dependent ● Time consuming ● Limited use in some organ systems
MRI	<ul style="list-style-type: none"> ○ No radiation exposure ○ Tomographic ○ Functional imaging 	<ul style="list-style-type: none"> ● Magnet is always on ● Expensive ● Not real-time
CT	<ul style="list-style-type: none"> ○ Detailed and accurate imaging ○ Real-time imaging ○ Able to image bone, soft tissue and blood vessels all at the same time 	<ul style="list-style-type: none"> ● Ionizing radiation ● Risk of serious allergic reaction to contrast material ● Expensive
PET	<ul style="list-style-type: none"> ○ Functional imaging ○ Gives nervous system details ○ Allows to study metabolic functions 	<ul style="list-style-type: none"> ● High cost ● Limited amount of time patient can undergo the procedure ● Poor resolution ● Cannot be repeated often due to high dose
OCT	<ul style="list-style-type: none"> ○ 3-D imaging ○ Detects difference on microscopic level ○ Does not require any subject preparation 	<ul style="list-style-type: none"> ● Small penetration depth ● Requires ideal positioning

1.2: Overview of imaging systems

The beam of X-rays before passing through the human body does not contain any important medical information. But as X-rays propagate throughout the patient they can tell a lot about the anatomical structure of a subject. The soft tissue and bones have different density and composition, so they attenuate X-rays in different ways. In addition, there are X-rays contrast media: iodine to visualize blood vessels and barium to enhance imaging of digestive tracts. When X-rays pass through the patient they undergo attenuation that varies spatially. There are a number of techniques that allow a visualization of the local alteration of X-ray beam intensity emerging from the human body.

First, imaging systems have utilized the fluorescent screen for conversion of ionizing radiation into light energy and then, X-ray film was exposed to this visible light to record the image. The single fluorescent screen was not thick enough to absorb most of X-rays and a significant fraction of them were just uselessly passing through a screen without being absorbed. It is not useful to make screen very thick to absorb more X-rays as then light scatters inside the phosphor resulting in considerable blurring and hence reduction in the image quality. A more effective usage of X-rays came with the development of a dual-screen cassette. Use of two screens improved the image quality because both screens were converting X-ray to light and the film placed between screens was illuminated from both sides improving contrast and making better use of the radiation. The fluorescent light emitted by the two screens was equalized by making the front screen thinner than the back, so that they would absorb the same amount of X-Rays (Figure 1.2).

The major reason of usage of two intensifying screens is to halve the blurring, while still providing good absorption of X-rays. In imaging modalities requiring high resolution (e.g. mammography), a single emulsion film is still used with a single intensifying screen [2].

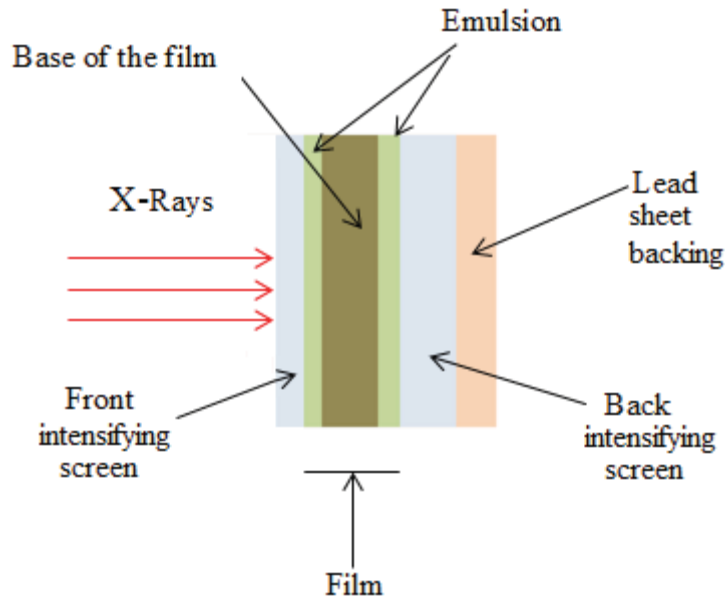


Figure 1.2: A scheme shows a double emulsion film sandwiched between two fluorescent screens. Such structure provides a more efficient usage of X-rays for making an image because film is illuminated from both sides making the image more intense (thickness not drawn to scale).

The X-ray image intensifiers (XRII) has been greatly advanced and utilizes a multistep conversion process in which the latent image was first carried by X-ray photons then by light photons, then by electrons and eventually by light photons (Figure 1.3). To provide such a complicated conversion scheme the XRII had a special design. An input fluorescent screen was mounted against a photocathode in such a way that when exposed to incoming X-rays, the input fluorescent screen starts to glow and causes a photocathode to emit low energy photoelectrons. On this conversion stage the intensity of incident X-rays was proportional to the intensity of emitted photoelectrons. After being emitted, the photoelectrons are accelerated towards the anode by an applied electric field. Electrostatic lenses are used for guidance and focusing of electrons towards an output screen. After the accelerated electrons strike the output fluorescent screen, it starts to glow many times brighter than the input one [2]. Such images could be observed not only directly by a radiologist using a mirror optical system but in a later development captured by a video camera and sent to monitor. A further development was to take the signal from the video camera and digitize it to make one of the first practical digital X-ray systems.

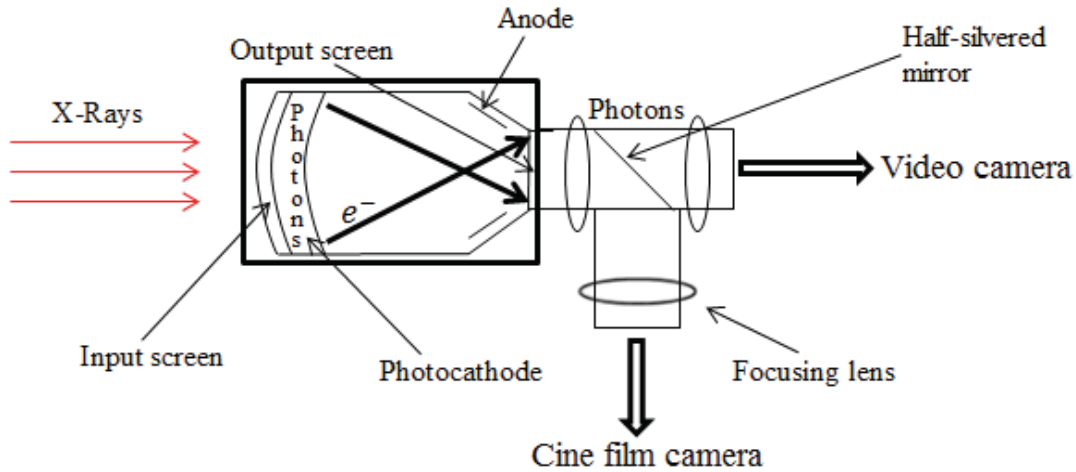


Figure 1.3: Figure shows a multistep conversion process from X-rays to optical image in the demagnifying X-ray image intensifier.

Over the past ten years, conventional XRII have started to be replaced by direct and indirect conversion active matrix flat panel imagers (AMFPI) which are now widely used for applications in X-ray medical imaging [22]. Currently, for radiography and fluoroscopy this technology is the state-of-the-art and allows digital image processing and computer-assisted diagnosis. Basically AMFPI consists of millions of individual electrical circuits integrated into detector elements called pixels. Each pixel consists of a thin film transistor, a charge collector electrode (direct conversion) or photodiode (indirect conversion) and a storage capacitor.

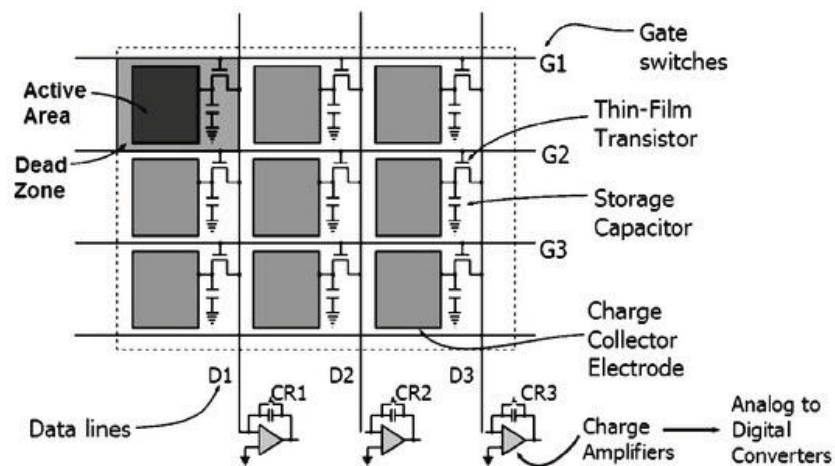


Figure 1.4: The scheme of a direct conversion AMFPI is shown.

The AMFPI has a row-column structure where a so called gate line connects pixels along one row and a drain line connects a column of detector elements through a thin film transistor (TFT) of each pixel. The gate line is used to address the pixel and the drain line connects a pixel with the charge amplifier. When the row is addressed, all the TFTs on that row are opened and the collected image charge flows from the pixel storage capacitor, through the drain lines, down to charge amplifiers and to analog-to-digital converters. During this operation the AMFPI is read out sequentially row-by-row [7]. Such a scheme offers significant improvements in the operational speed of the imager as the latent charge image is read out not element-by-element, but the whole row at once. This makes it a good candidate for fluoroscopic applications where images are acquired with frequency of 30 frames per second, meaning that all detector elements must be read out in less than 33 ms [4].

Utilization of flat-panel technology for X-ray systems has revolutionized digital X-ray imaging. The major advantages of flat panel technology are that it may cover large areas (40"x40"), fast read-out, and compactness in thickness.

1.3: Analysis of modern X-ray to charge conversion techniques

As we concluded above, flat-panel imager systems are the most mature and up-to-date system. Another important issue is to have a proper detection media that will provide the best X-ray sensitivity and will allow one to reduce the dose of radiation that is so crucial for medical applications. Most commercially available active-matrix flat-panel imagers nowadays utilize so-called indirect conversion approach. This implies two-step conversion process from X-ray to detectible electric signal.

1.3.1: Indirect conversion detection

The indirect conversion scheme is called indirect because the conversion of the X-ray to the electrical signal is performed with involvement of an intermediate step where by an X-ray is converted first to visible light and only then to the electrical signal. This scheme is presented in Figure 1.5.

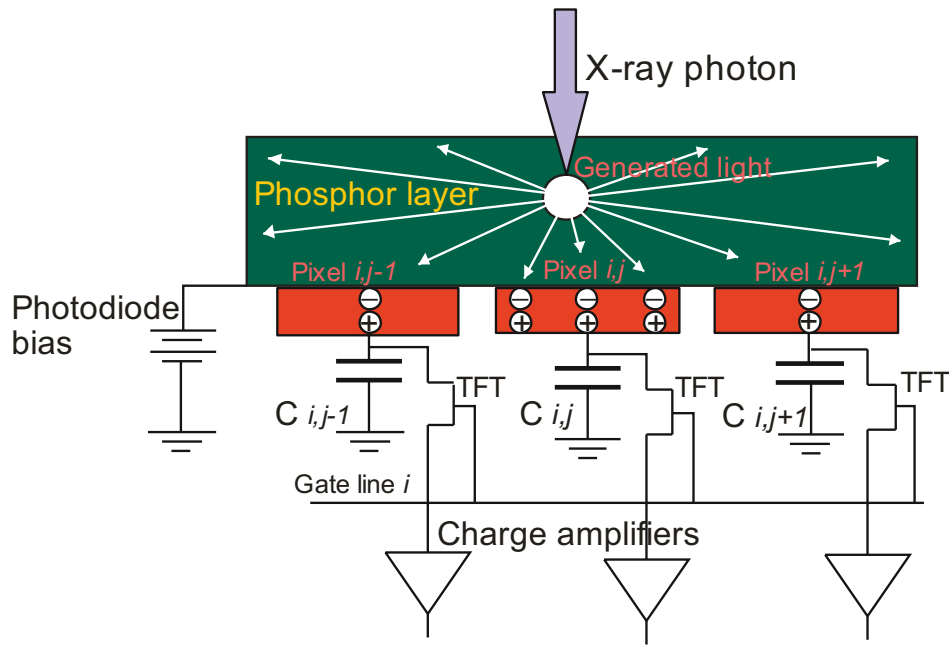


Figure 1.5: The indirect conversion scheme is shown. The absorbed X-rays generate light that disperses in a scintillator. An array of photodiodes is required to convert the light photons to electric signal.

Within such an indirect conversion scheme, in the first conversion stage each absorbed incident X-ray photon (~ 50 keV) is converted into many photons of visible light (~ 2 eV) by a scintillator, - a material that emits light when exposed to radiation [6]. The intensity of the visible light is proportional to the intensity of X-rays. The wavelength (energy) of emitted light is usually blue or green and depends on the phosphor material. The scintillator is optically coupled to an active matrix array. When X-ray is absorbed by scintillator layer, it creates a whole burst of optical photons which are guided by the columnar structure of the scintillation crystal toward the imaging matrix where it can be collected. Every pixel of the indirect conversion AMFPI must have a photodiode that converts light into measurable electric signal. The latent-charge image is stored at the pixel capacitors and when the pixel is addressed, the charge is read out. The operational principle of the scintillation crystal is shown in Figure 1.6.

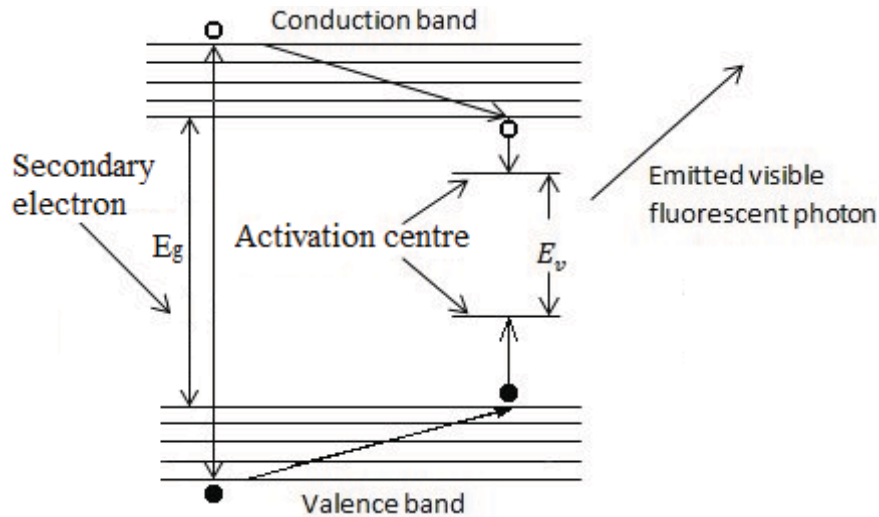


Figure 1.6: A band structure shows the operational principal of the scintillator. The electron-hole pair generated by the X-ray is relaxed to the energy levels created by the activation centers (created by adding impurities). Following recombination of the electron and hole trapped at the activation center occurs with emission of the characteristic visible light photon. The wavelength of the characteristic photon is defined by the band gap of the activation centers E_v . E_g is the host (phosphor material) band gap.

The energy of the absorbed X-ray photon creates high energy electron which in turn interacts with matter of the scintillator is transferred to bound electrons of the crystal atoms. If the transferred energy is higher than the band gap (E_g) an excited electron will enter the conduction band and be free from the binding forces of the parent atom. After the excited carriers lose excess energy, they relax back to the ground state. This process is accompanied with reemission of a photon in the visible region of the electromagnetic spectrum. The energy of output photon can be adjusted by means of introduction of small amount of activator impurity to the scintillator, so that that it creates specific energy states inside in the band gap – activation center. In this case the photon is emitted as result of interband transition of carriers. Some scintillators use only the intraband transition of electrons to initiate the photon emission.

One of the disadvantages of this indirect conversion is the light scattering in the scintillation crystal. The fundamental limiting factor of a phosphor is that it isotropically emits light photons in all directions. The light spreading inside the phosphor layer is

shown in Figure 1.7. Even though a pillar-like structured cesium iodide (CsI) scintillator is used for channeling light, it still spreads in all directions. If light spread is significant, light would be collected not only by the one pixel above which it was generated, but by several neighboring pixels as well, thereby leading to significant degradation of the spatial resolution.

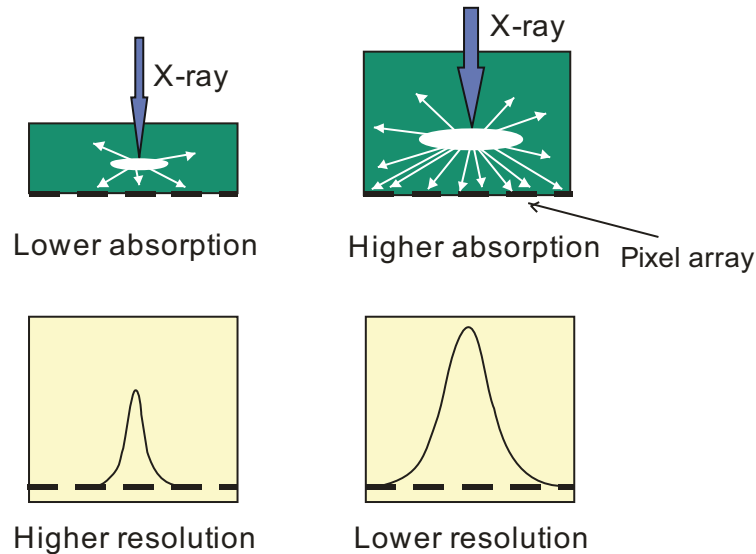


Figure 1.7: The figure shows detrimental effect of light spreading on spatial resolution. The effect of light spreading becomes more pronounced with increase of the scintillator thicknesses.

The structured CsI scintillators possess much higher spatial resolution in comparison to powder screens ones, but its guiding capabilities are still poor due to structural and mechanical defects [6]. In order to get a more sensitive detector we need a thick layer of scintillator. However, as we have seen an increase in phosphor thickness results in higher image blurring and impairs the spatial resolution. This effect is especially pronounced in case of very penetrating X-ray energy. So, there is always a tradeoff between quantum efficiency and spatial resolution.

Another disadvantage of indirect is the multi-step conversion process applied to convert X-ray to electrical signal. Although CsI is highly efficient, there are losses of signal involved at every conversion step: poor conversion efficiency of the X-ray to

visible photon energy, imperfections in the scintillator column surface. As a result the X-ray to visible light energy conversion efficiency for CsI is about 15%. All these flaws of the indirect conversion approach become more pronounced with reduction of the X-ray exposure and at very low doses of radiation the detector performance is limited by electronic noise, not by the quantum noise of the detector.

1.3.2: Direct conversion detection

The problems identified in the indirect conversion scheme can be resolved with an alternative detection scheme called direct conversion. It uses a layer of photoconductor for conversion of an incident X-ray into electron-hole pairs (EHP) to be a single-step approach. The conversion efficiency of detector is then defined by the number of EHPs created by one absorbed X-ray photon. The more EHPs created from an X-ray, the higher the sensitivity of the detector. The rest of the imager read-out scheme remains unchanged compared to indirect conversion AMFPI. Direct conversion offers several major advantages over the indirect conversion approach. First, it eliminates the use of scintillation crystal. X-rays are converted into electric signal directly, without any intermediate steps. This permits much higher conversion efficiency. Secondly, the spatial resolution is limited only by the pixel size of the detector, because the EHPs move along the lines of applied electric field toward the opposite electrodes. There is no significant latent image charge spreading due to carrier scattering. The magnitude of charge collected on the capacitor is proportional to the X-ray beam intensity. The schematic representation of the direct conversion approach is shown in Figure 1.8.

In the direct conversion scheme, the spatial resolution is primarily limited by fundamental X-ray interaction physics. Usually this is the inherent range of the primary photoelectron in contrast to indirect approach where resolution is limited by an optical spreading effect in the phosphor. Therefore, increasing the photoconductor thickness would improve the quantum efficiency of the detector due to a rise in the absorption of X-ray without sacrificing the image quality, as it was the case in indirect conversion-based AMFPIs showing the image degradation.

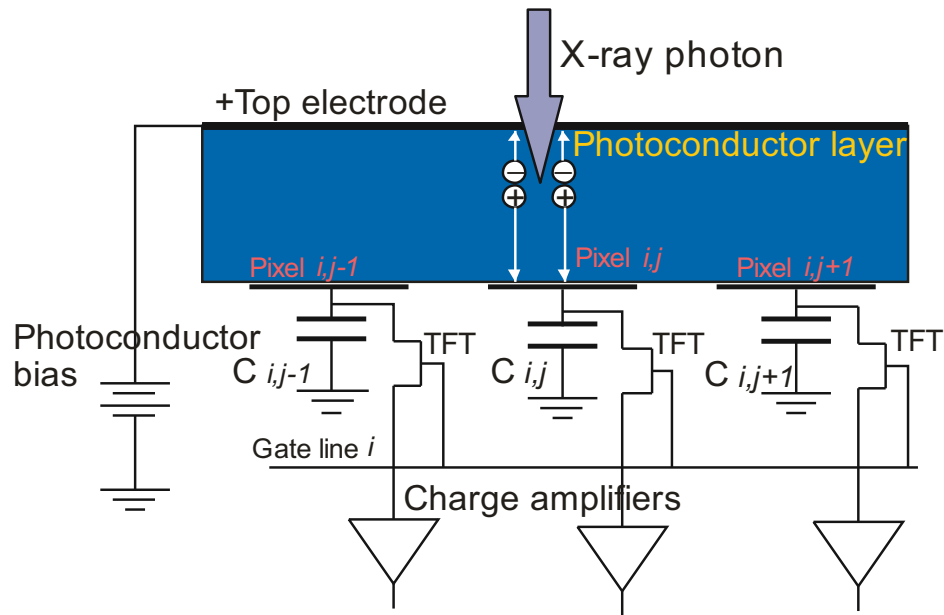


Figure 1.8: Scheme shows the operation principle of direct conversion-based imager. When incident radiation is absorbed in the thickness of a photoconductor, it generates charge carriers that move along the lines of applied electric field.

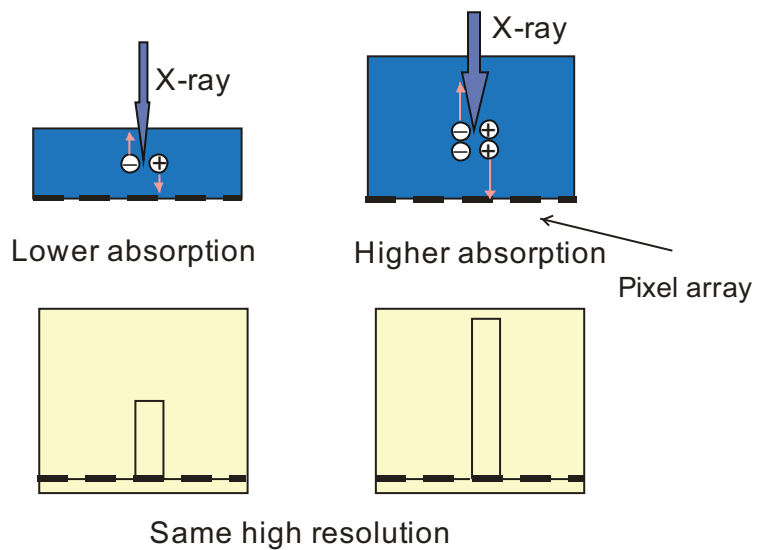


Figure 1.9: Scheme shows that for direct conversion case an increase in photoconductor thickness does not induce the degradation of the spatial resolution.

1.3.3: X-ray Light Valve System

Although active matrix flat panel imagers provide high performance, they are very expensive and there is a need for lower-cost digital imaging systems for general applications in radiography. A read out system called an X-ray Light Valve (XLV) has the potential to satisfy the needs of digital radiology and offers higher resolution than flat-panel detectors, while reducing the cost due to the simplicity of the design [9].

The XLV detector consists of three main components: photoconductor, liquid crystal (LC) and optical scanner. The photoconductor is physically coupled to the liquid crystal and optical scanner. The system utilizes a liquid crystal light valve as a light modulator. The properties of liquid crystals are employed to control the light propagation through an optical assembly. The photoconductor is used as a detection media and X-ray-to-charge transducer, the liquid crystal serves as an analog display while the optical scanner is used for image digitization [20]. The concept is shown in Figure 1.10.

Under exposure to X-rays, the photoconductor generates EHPs. The applied electric field provides a collection of the generated charge carriers at the interface of the photoconductor and liquid crystal. This causes the LC to change its molecular arrangement thus creating the latent image. Next a patent image is obtained on the liquid crystal, by use of external illumination, polarizer, analyzer and the optical scanner are used to read it out. There are two general modes of operation for XLV systems: reflective and transmission. The reflective mode was shown to have significant advantages over the transmission one. Transmission mode requires the usage of large lenses for image focusing and read out light and charge coupled device (CCD) must be placed on the opposite sides of XLV. This would make a device very bulky and not very cost-effective. In the reflective configuration the read-out light and read out electronics are placed on the same side while CCDs and all cumbersome optics are replaced by a single scanner, thus making the scheme light and less costly.

The mechanism of the charge photogeneration and collection in XLV is similar to that in direct conversion scheme where X-rays are absorbed by a photoconductor and generate electron hole pairs (EHP) which then drift along the lines of electric field

towards the opposite electrodes. The variation of charge density in the photoconductor mimics the variations of X-ray intensity. During this phase high voltage is applied to both the liquid crystal and photoconductor material. As shown in Figure 1.10 a, the charge is collected at a bias electrode from one side and at the liquid crystal-photoconductor interface at the other side. As there is no electrode for charge exit from LC side, the collected charge becomes trapped at the interface. When an external electric field is turned off the trapped charge make the LC molecules tilt and this changes the light propagation through the liquid crystal, creating the image. The variation of collected charge density on the interface is proportional to the variation of the light intensity passing through the liquid crystal. After the modulated latent image is received on the LC (Figure 1.10 b), it is read out and digitized by the scanner. The energy of the read out light photons is chosen to be less than the band gap of a photoconductor, so that no charge is photogenerated. After an image is taken, it needs to be erased before making a new exposure. In order to reset the XLV, the photoconductor is flooded with an erasing light. In contrast to the read out illumination, the energy of erasing light is higher than the photoconductor's band gap. Therefore, photogenerated EHPs neutralize the residual trapped charge and resets the photoconductor for the next image.

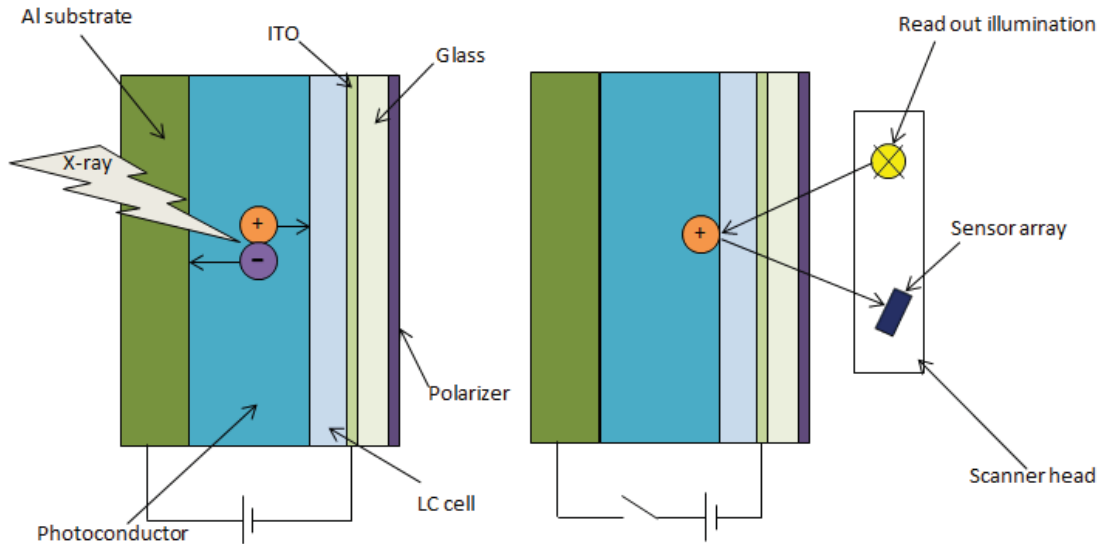


Figure 1.10: The principle of XLV operation is shown. (a) The absorption of the X-ray radiation results in charge generation. The electron-hole pairs are collected on opposite sides of the XLV structure. (b) Trapped charge on the interface of photoconductor and LC causes the changes in light transmission through the liquid crystal cell.

The liquid crystal is designed in such a way that it works as a quarter-wave plate for the wavelength of the read out light. When there is no bias applied to the LC cell it is a dark state of operation. The bright operation state is initiated by the voltage applied to a cell which tilts the molecules. The more charge is trapped at the LC/photoconductor interface the higher will be intensity of the reflected light. The dynamic capabilities of the XLV system is limited by the read-out speed of the scanner.

The read-out time of one image is usually about 1 frame per minute, which is not suitable for fluoroscopic applications (30 frames/second [4]). However it is a good candidate to be a low-cost radiographic system.

1.4: Attenuation of an X-ray beam by a medium

Direct conversion detectors have potential for medical imaging applications. The properties of the radiation detection media are a crucial factor that defines the performance efficiency of whole detector. The transfer of ionizing radiation energy to the sensor is based on the complex interaction of X-ray photons with the atoms of an absorber. This demands more attention to the nature of these processes in order to select the most appropriate photoconductive material to insure its successful performance in an X-ray-to-charge transducer used in direct conversion detectors.

When X-rays pass through any material they might just go through or be attenuated (Figure 1.11). The probability that an X-ray photon will interact with the absorbing medium depends on several factors, namely: energy of a photon, material thickness and composition of the absorber. The amount of radiation attenuated by an absorber of a given thickness is defined by the attenuation coefficient of absorber. The process of the X-ray beam attenuation is a removal of X-ray photons from the incident beam as it passes through the material as a result of absorption of photon energy or scattering events. There are two attenuation coefficients that are usually used to characterize the ability of material to attenuate the X-rays. Their names are dictated by the units of measurements they are linear and mass attenuation coefficients.

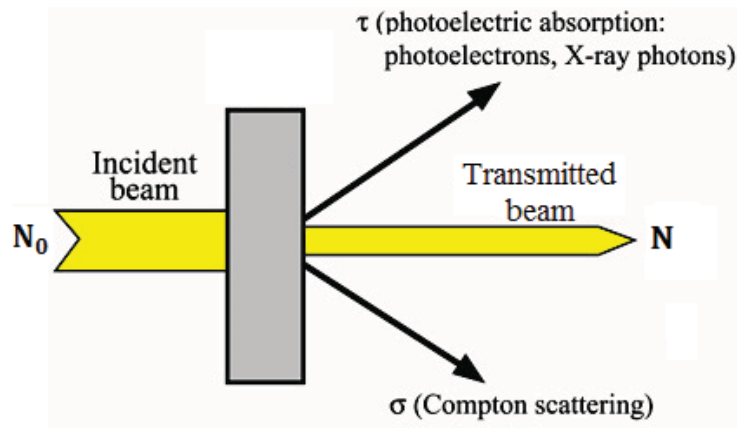


Figure 1.11: Attenuation of the input beam by a material.

Linear attenuation coefficient is used to express how much incident monoenergetic beam of X-rays is attenuated by a centimeter of absorbing medium. If we consider an incident X-ray flux intensity to be N_0 while N to be assigned to the transmitted intensity, then for a given thickness of the material d , the transmitted intensity is determined as:

$$N = N_0 e^{-d\mu_l}, \quad (1.1)$$

Here e is the base of natural logarithm and μ_l is the linear attenuation coefficient measured in cm^{-1} . The minus sign accounts for a reduction in the beam intensity as thickness of the absorber increases [2]. The linear attenuation coefficient (μ_l) depends on density, number of electrons and, therefore atoms in the slab and is defined for specific X-ray energy ε . For example in the case of water, the linear attenuation coefficient is proportional to the density of physical state. Thus, water vapors, liquid water and ice would have different μ_l .

Another way to express the attenuation of the incident beam intensity as it propagates through the medium is mass attenuation coefficient μ_m . The mass attenuation coefficient is determined by dividing linear attenuation coefficient by the density of the absorber and is measured in $[\text{cm}^2/\text{g}]$:

$$\mu_m = \mu_l / \rho \quad (1.2)$$

where ρ is the density of the absorbing medium. Mass attenuation coefficient depends on the absorber atomic number and photon energy and does not depend on density of the material [1]. Thus, all three physical states of water have the same μ_m .

1.5: Physics behind the radiation detection techniques: types of interaction of radiation with matter

For the X-rays used in diagnostic medical imaging with photons in energy range 30-150 keV, there are three basic mechanisms of radiation interaction with matter. They are:

1. Photoelectric effect
2. Compton scattering
3. Rayleigh (coherent) scattering

The type of interaction of ionizing radiation with matter depends on the energy of the X-ray photon and the medium.

1.5.1: Photoelectric effect

The photoelectric effect occurs when incident X-ray photon interacts with electrons. As a result of the interaction, the photon disappears and all its energy is used to eject one of the electrons from the atom's orbital. The electron that is free now is called a photoelectron (see Figure 1.12).

Much of the photon's energy is used to overcome the binding energy of the parent atom and the residual energy is transferred into kinetic energy of the photoelectron:

$$E_0 = E_b + E_e \quad (1.3)$$

where E_0 is the energy of X-ray photon, E_b is the binding energy of the orbital E_e is a kinetic energy of the ejected photoelectron.

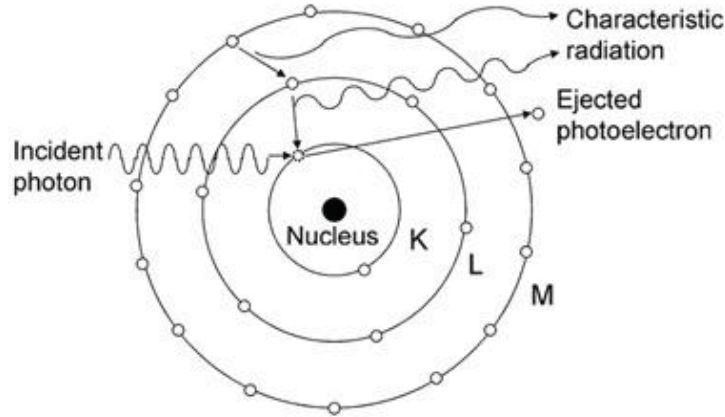


Figure 1.12: The X-ray photon interacts with an innermost electron and gives all of its energy to the electron. The electron is then ejected from the atom using some of its energy to overcome the attractive forces of a positively charged nucleus. The vacancy left by the photoelectron is filled by an electron from an outer shell. Process of transmission of the electron from an outer shell to inner one is accompanied with emission of characteristic X-ray photon.

The photoelectric interaction will take place only if the energy of the incident photon is higher than the binding energy of the electron ($E_0 > E_b$). Otherwise, such interaction is not energetically feasible and will never occur. The probability of the photoelectric effect is highest when the photon's energy is equal to the binding energy of electron ($E_0 = E_b$) [4].

The attenuation of a photoelectric reaction is important process of X-ray interaction with medium, and photoelectric attenuation coefficient is proportional $\mu_{P.E.}$ to the third power of the incident photon energy ε and inversely proportional to the third power of atomic number Z of absorber [1]:

$$\mu_{P.E.} \propto Z^3 \propto \frac{1}{\varepsilon^3} \quad (1.4)$$

The ejection of a photoelectron is not a single step process but triggers a cascade of electron transitions. As any physical system tends to be at the lowest possible energy state, the vacancy in the inner orbital is immediately filled with an electron from one of the outer orbitals of an atom and less frequently by the electron of the neighbor atom [1]. When an outer electron fills the vacancy a photon of characteristic radiation is emitted.

The energy of the emitted radiation is equal to the difference in binding energy of orbitals participating in the transition process (between outer-shell orbital donating electron and inner-shell electron providing a vacancy) and depends on the material. For example during transition of an electron from L to K orbital, the energy of emitted characteristic photon is

$$h\nu = E_K - E_L \quad (1.5)$$

where E_K and E_L are binding energies of K and L orbitals respectively.

Usually the vacancy in L shell is filled by an electron from the M shell, vacancy in M shell by electron from outermost orbital and so on, until all binding energy of the K-shell electron knocked out from the orbital by incident photon is converted into photons. The most energetic characteristic radiation is emitted when a free electron fills the void in K-shell.

We already mentioned above, that for the high atomic number materials the photoelectric interaction with the inner shells electrons would only occur if X-ray has enough energy to overcome the binding forces of a parent atom. If the energy of the incident photon is higher than the binding energy of the electron ($E_0 > E_b$) the transmission of X-ray beam actually drops with further increase in beam energy, i.e. transmission of X-ray is highest at $E_0 = E_b$. In the figure below (Figure. 1.13) the mass attenuation coefficient is plotted versus incident electromagnetic wave energy for different absorption mediums.

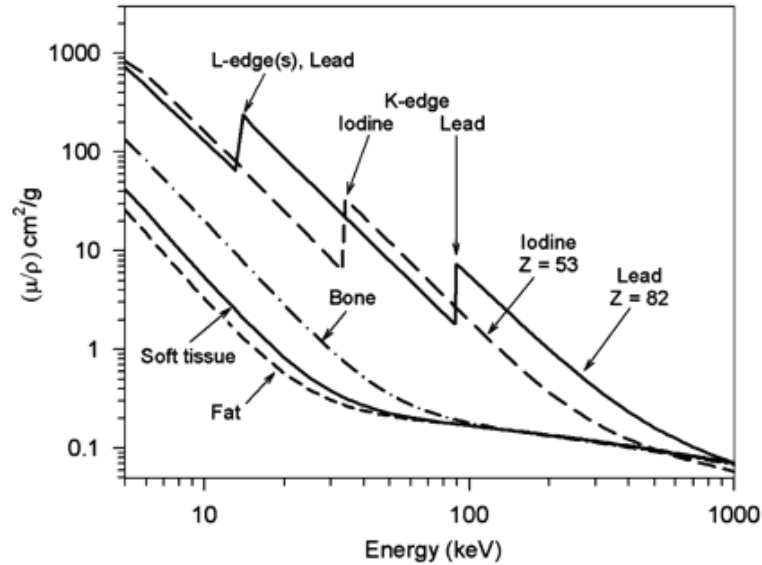


Figure 1.13 Mass attenuation coefficient (μ_m) for several materials are plotted as a function of incident photon energy ε [5].

Lead (Pb) is a good example to represent the behavior of the mass attenuation coefficient for different X-ray energies. In Figure 1.13 the graph of Pb shows a gradual decrease in attenuation that is approximately inversely proportional to the third power of the photon energy. However, at energy of 88 keV, there is a sharp rise in absorption which is called the K-edge and equal to the binding energy of the K-shell electron. Below that energy the photon cannot eject a K-electron, and the photoelectric effect can only occur with electrons on L and M levels. Therefore, in the energy range from 20 keV to 88 keV, the transmission of X-rays through the material (Pb) grows but just above 88 keV, there is a sharp decrease in transmission due to the increase in attenuation by a factor of ~ 5 followed by ejection of a K-electron. With further increase in ε the attenuation coefficient μ_m decreases and transmission of radiation starts to grow again [1].

For low- Z materials like tissue or bone, the K-shell binding energy is only few keV (0.5 keV in oxygen and 4 keV in calcium) and therefore low-energy characteristic X-rays will be locally reabsorbed. However, for high atomic number materials used in direct and indirect conversion with K-shell energies in the range of 30-150 keV, the characteristic

photon is reasonably energetic and can travel finite distance or even might escape from absorption medium [4].

1.5.2 Compton (Incoherent) scattering

Compton scattering is a type of interaction of radiation with matter when a high energy incident photon incoherently collides with the loosely bound electron on the outermost shell. In contrast to photoelectric effect, incident photon does not disappear completely but always retains some fraction of the energy (Figure 1.14).

The incident radiation energy is used for ejecting an electron from the orbital and extra portion of unused energy is transferred into kinetic energy. The incident photon retains the residual part of the energy and deflects from the original trajectory on some angle θ as a scattered photon. The liberated electron is called a recoil electron and has energy [1]:

$$E_r = E_0 - E_{sc} \quad (1.6)$$

where E_0 is the energy of X-ray incident photon, E_{sc} is the energy of the deflected photon, E_r is the energy of the ejected recoil electron.

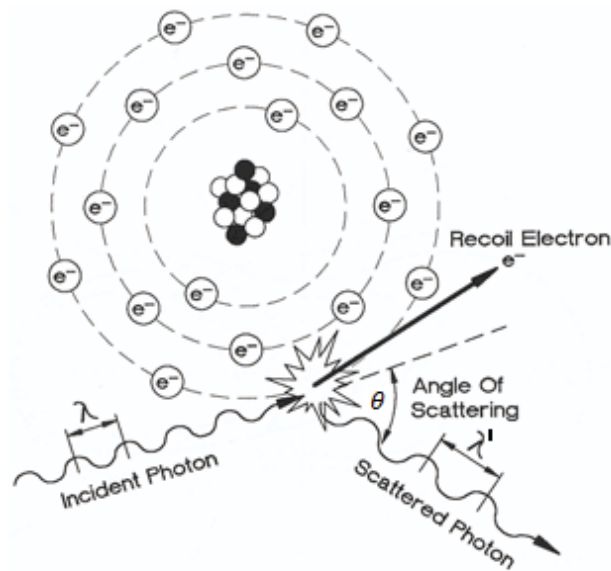


Figure 1.14: A photon interacts with electron on the outermost shell. As a result of interaction an electron is ejected and the photon is scattered at some angle thus changing the trajectory and wavelength [50].

Usually Compton scattering occurs when an incident X-ray has a much higher energy than the binding energy of the electron and the interaction looks like a collision of two billiard balls, one of them is the cue ball and another is in the rest state. The energy of the recoil electron is related to the scattering angle by a relation:

$$E_r = E_0 \frac{\alpha(1-\cos\theta)}{1+\alpha(1-\cos\theta)} \quad (1.7)$$

$$\alpha = \frac{E_0}{m_0 c^2} \quad (1.8)$$

where m_0 is electron rest mass and c is speed of light. Parameter α is a coefficient that shows the ratio between incident photon energy and energy of electron in the rest state ($m_0 c^2$). The energy of the scattered photon is calculated with the Klein-Nishina equation [4]:

$$E_{sc} = E_0 \frac{1}{1+\alpha(1-\cos\theta)} \quad (1.9)$$

As angle of scattering (θ) increases, the energy of scattered photon decreases. This phenomenon becomes more pronounced at high photon energies.

From the equations above it is seen that recoil electron will acquire the maximal energy and the scattered photon will have the minimal energy if an incident X-ray makes a direct hit and gets backscattered [2]:

for $\theta = 180^\circ$, $\cos\theta = -1$:

$$E_r^{max} = E_0 \frac{2\alpha}{1+2\alpha} \quad (1.10)$$

$$E_{sc}^{min} = E_0 \frac{1}{1+2\alpha} \quad (1.11)$$

On the other hand the energy transferred to the recoil electron will be minimal in case of grazing collision. In this case the photon will retain most of its energy and electron will emerge at almost 90° with respect to the photon's trajectory:

for $\theta \approx 0, \cos\theta \approx 1, (1 - \cos\theta) \approx 0$:

$$E_{sc}^{max} \approx E_0, E_r^{min} \approx 0. \quad (1.12)$$

The probability of Compton scattering depends only on the number of electrons per gram, as interaction occurs between incident photon and free electrons (for the diagnostic energies of X-rays the electron is considered to be free if the binding energy is less than 1 keV).

All chemical elements have comparable numbers of electrons per gram [4]. This implies that the probability of Compton reactions do not depend on Z and is defined mainly by the incident radiation energy [1]. However, more energetic photons have much higher probability to scatter in the forward direction, whereas low energy photons are generally scattered isotropically [1] as it is seen from the Figure 1.15. This is accounted by the fact that high energy photons have a higher momentum and, therefore they are deflected less after interaction with electron from the initial direction. Photons with energies about 1 MeV are usually forward deflected, but these photons are out of the energy range used in the medical imaging applications.

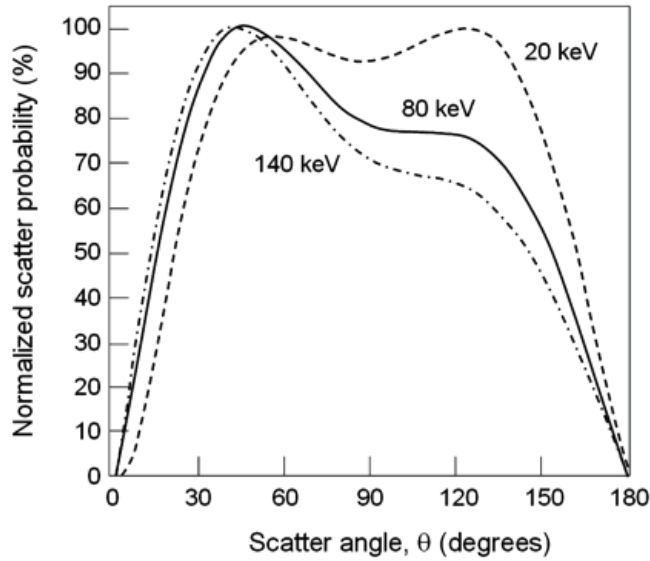


Figure 1.15: The scatter distribution probability is plotted as function of a deflection angle relative to incident photon direction [51].

Compton scattering is the main mechanism of radiation scattering in the diagnostic radiology. The scattered photon is almost as energetic as primary. So, during a medical diagnostic procedure, like fluoroscopy, the energetic photons might deflect from the initial trajectory directed to the patient and affect the medical personnel. Therefore, the scattering during X-ray imaging examination can result in a high total accumulated dose and has harmful effect not only to the patient, but to the medical staff as well unless they are properly protected.

1.5.3 Rayleigh (Coherent) Scattering

Elastic scattering of an X-ray and an atomic electron is called Rayleigh (coherent) scattering. When an incident photon interacts with atomic electrons it makes them oscillate. Vibrating charged particles emit electromagnetic radiation. Due to a much higher mass of an atom than that of a single electron, there are no essential losses in the recoil energy during an elastic interaction (Figure 1.16) [4].

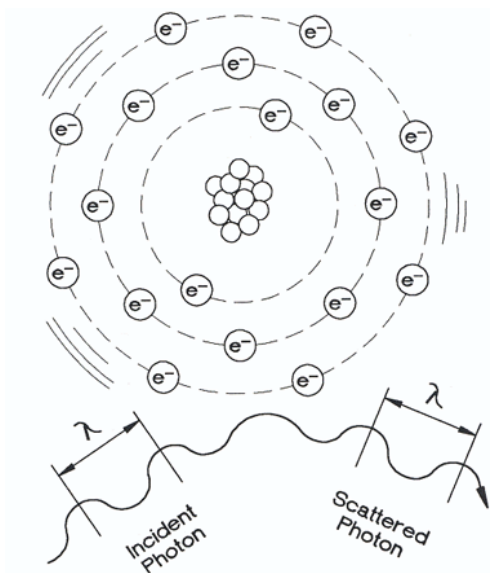


Figure 1.16: This figure shows the coherent scattering of incident photon with outer shell electron in atom. For coherent scattering the wavelength of the incident and scattered photon remains unchanged [50].

The energy of an incident and a scattered photon is very much the same as $E_0 = E_{sc}$ and there is no ionization of medium. In a coherent reaction, the photon gets deflected

from its original trajectory and may escape from the material or be absorbed at some distance from the position of the primary photon absorption. This causes additional limitations of detection accuracy. The deflection angle depends on the photon energy. With an increase of a photon's energy it becomes harder to deflect them from initial trajectory, but in contrast to Compton scattering, an elastic or coherent scattering has a very little probability of backscattering (figure 1.17).

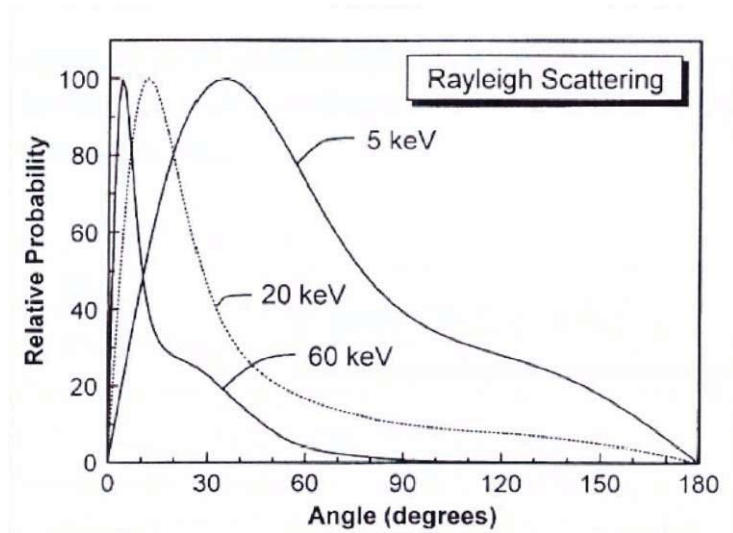


Figure 1.17: The Rayleigh scattering deflection probability for several energies of X-ray photon versus scatter angle is shown. The probability of backscattering is lower in comparison to the Compton interaction [4].

There are three more types of radiation interactions with matter that are out of diagnostic radiology energy range, but worth mentioning. They all have critical energies ε_t below which they do not occur at all. We will discuss them in order of increasing ε_t . The first is called a pair production interaction with $\varepsilon_t = 1.022 \text{ MeV}$. When pair production takes place the energetic photon interacts with the nucleus of an atom. As a result of such an interaction an incident photon gets completely absorbed and disappears, but a positive-negative electron pair is created. Since two electrons are formed and each electron has the rest mass of 0.511 MeV , the reaction becomes feasible only if photon's

energy exceeds 1.022 MeV. The excess energy of a photon is transferred into kinetic energy of electron pair [3]:

$$E_+ + E_- = E_0 - 2m_0c^2 = E_0 - 1.022 \text{ MeV} \quad (1.13)$$

The emitted positron is traveling within the material, losing its energy in collisions with other atoms. After all the kinetic energy is dissipated, the positron interacts with an electron and the two charged particles annihilate. As a result, two gamma rays are emitted in opposite direction with energy of 0.511 MeV. The excess energy is shared between electrons in random proportions. Sometimes energy is equally split between two particles and sometimes only one particle absorbs all the energy. But generally the division of energy is in the 20-80% sharing range [2].

When the incident radiation exceeds $4m_0c^2 = 2.044 \text{ MeV}$ another type of interaction called triplet product becomes possible. In contrast to a pair production, an incident photon interacts not with the atomic nucleus, but with atomic electrons. When the photon disappears, its energy is used to create an electron, positron and beta-particle [4].

The photon with energy higher $\varepsilon_t = 7 \text{ MeV}$ may undergo a photodisintegration reaction. A result of photon-atom collision is ejection of a neutron, a proton, an alpha particle or cluster of particles from the atom [1].

All listed above processes represent different mechanisms of X-ray beam attenuation as a result of photon energy transferred to the material. The only exception is Rayleigh interaction because here the scattered photon has the same energy as the incident photon and no energy is transferred to the material. But for this type of interaction the incident photon changes the trajectory and in this way is removed from the beam. The linear attenuation coefficient accounts for the net change in the beam intensity including both absorption and deflection of incident radiation. For the diagnostic energy range (30-150 keV) it is equal to the sum of probabilities of all possible types of interactions [2]:

$$\mu = \tau + \sigma_{coh} + \sigma \quad (1.14)$$

where τ is an attenuation due to photoelectric effect, σ_{coh} is an attenuation due to Rayleigh scattering, σ is a Compton attenuation coefficient, π -attenuation resulted from the pair production effect.

1.6: PbO for direct conversion detectors

The linear attenuation coefficient versus photon energy is plotted for different materials used for radiation detection in X-ray medical imaging in Figure 1.18 [21]. As it is seen from the figure above, Lead Oxide (PbO) has higher attenuation coefficient than other materials used for radiation detection in medical imaging.

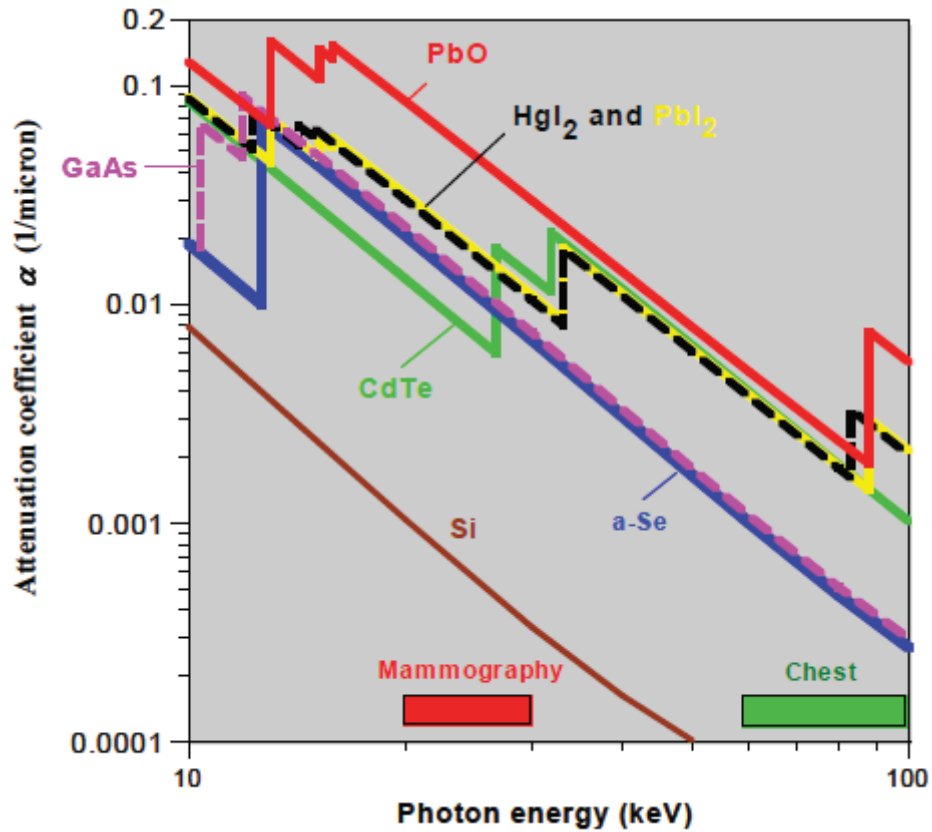


Figure 1.18: The dependence of the attenuation coefficient on X-ray energy is shown for different photoconductors [21].

For such high-Z material as PbO, most of input energy within diagnostic energy range would be attenuated by the photoelectric interaction. The other advantage of PbO over

other candidates for direct conversion detectors is the absence of heavy *K*-edge absorption edges on the diagnostic range up to 88 keV, so most of the absorbed energy would be transferred into kinetic energy of the photoelectron. This fact also benefits to the image quality as the image blurring from the reabsorption of characteristic photon would be minimal [4].

Although, PbO has long history of application in optical imaging and it was shown that PbO is one of the best candidates for applications in X-ray medical imaging [24], the fundamental properties of PbO are still not established firmly. This work is dedicated to addressing this issue and to provide us with basic X-ray parameters of PbO (charge yield, carrier mobility and the dark current) as well as the details of improved fabrication process for Lead Oxide.

Chapter 2: Fabrication process and morphological analysis of PbO

This Chapter describes the details and improvements of the PbO fabrication process required to grow the relatively thick layers needed to absorb X-rays efficiently. The morphology of the PbO layers was investigated with both optical and scanning electron microscopy whereas their composition is examined with help of Raman spectroscopy [26, 27, 28]. The characterization of the structural and photoelectric properties of PbO samples will also be shown.

2.1: Background of PbO deposition

In the literature, most data concerning the structure of PbO-layers is based on the research by Philips of “Plumbicon”- vacuum video tubes. Already in the early sixties, Philips had started development of deposition technology of PbO films, which was used as the light sensitive target of these TV-broadcast-tubes. The Plumbicon layers consisted of thin platelets ($2\ \mu\text{m} \times 0.5\ \mu\text{m} \times 5\ \text{nm}$) and are assembled in a very porous, polycrystalline structure with less than 50% packing density. The size and orientation of the platelets were found to vary during deposition. The industrialized Plumbicon used a substrate process temperature of $120\ \text{°C}$ [14].

The thickness of Plumbicon films was $\sim 10\text{-}20\ \mu\text{m}$, which was enough to provide efficient absorption of the visible light photons, but for good absorption of diagnostic X-ray photons the thickness of the photoconductive layer should be about ten times greater [4]. The thin PbO layers used in vacuum tubes had a very good photoconductive performance which therefore suggests an idea that thick layers of PbO would also provide a good X-ray performance.

The PbO layers are built of *platelets* which are packed together. There is a lot of space between the individual platelets that results in the formation of a porous structure. Along the direction of the sample growth, micromorphology changes in terms of the

platelet dimensions (lateral as well as in thickness) and orientation. On the substrate interface region the platelets appear smaller and more or less oriented in the growth direction, but in the bulk of the film the individual platelets are oriented perpendicular to each other with an angle of $\sim 45^\circ$ to the growth direction. The presence of a large fraction of small platelets is confirmed with the optical microscope image of the surface (Figure 2.1 a) as well as the Scanning Electron Microscope (SEM) picture of a cross-section surface (Figure 2.1 b) obtained by fracturing an evaporated sample. The platelets are found to be around 100 nm thick and have diameters of a few μm .

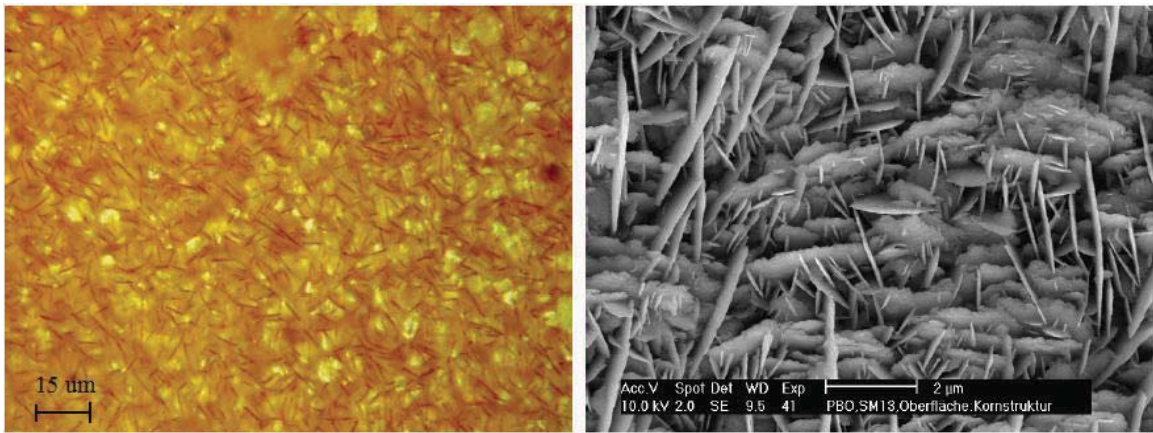


Figure 2.1: a) Picture of the PbO layer surface taken with optical microscope [13] b) Picture of the fracture of PbO film taken with SEM [13]

The uniformity in the layers has a pronounced dependence on the substrate temperature which is shown in Figure 2.2. At relatively low temperatures of up to 80°C , it is seen that platelets are arranged into circular structures called “nodules”, whereas at $\sim 150^\circ\text{C}$ we get more homogeneous layers. Another undesirable effect that occurs at the lower temperatures are cracks. Their appearance may be explained by nodule formation and can be avoided in a certain substrate temperature range from 95 to 125°C (Figure 2.2). Therefore, maintaining a substrate temperature within a certain temperature window is essential in order to obtain uniform layers.

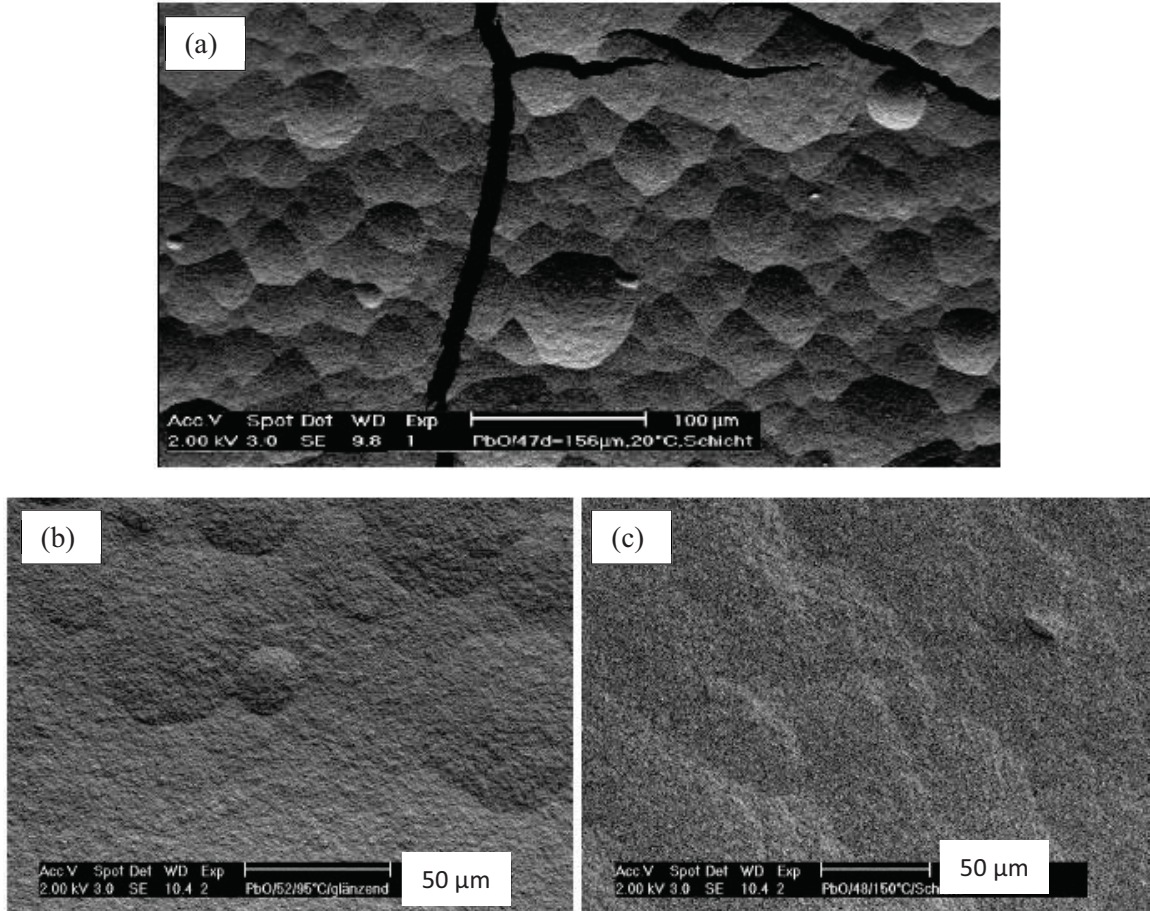


Figure 2.2: Pictures of PbO surface grown at the different substrate temperatures and taken with SEM: a) Substrate temperature is $T=20\text{ }^{\circ}\text{C}$, b) $T=95\text{ }^{\circ}\text{C}$, c) $T=150\text{ }^{\circ}\text{C}$. [13]

The PbO-layers are very porous with a packing density below 50 %. The porosity is determined by weighing layers of a known area and measuring its thickness. Thus comparison of the estimated density from these measurements with the known crystalline density of PbO (9.53 g/cm^3) can provide an evaluation on the sample porosity. The cross-section SEM pictures of a PbO-layer were taken at three different vertical positions (SEM pictures taken on the different layer depth are presented in Figure 2.3). A decrease of packing density from bottom (first layer formed) to top (last layer) could be identified is visually apparent.

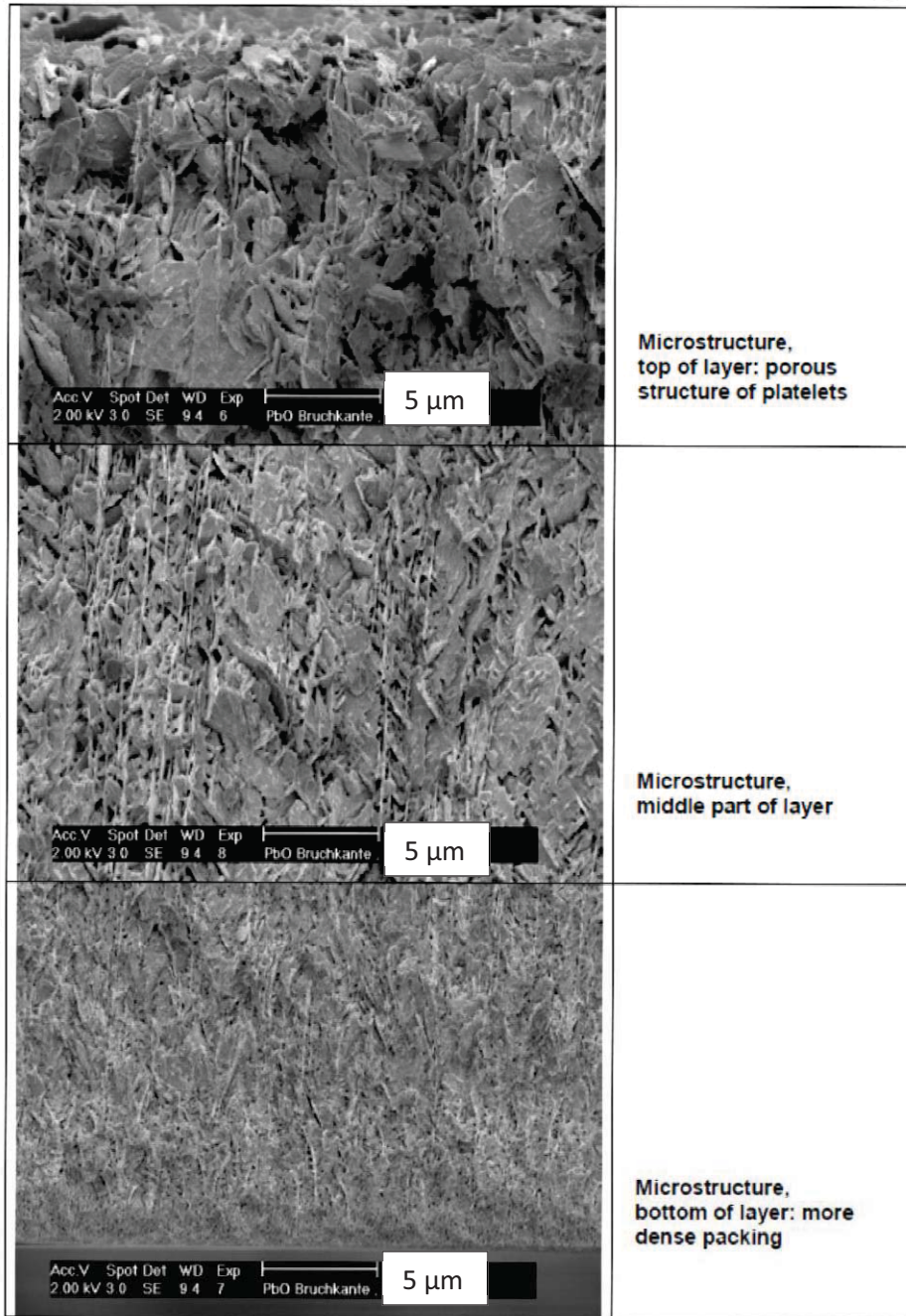


Figure 2.3: The change of packing density within the depth of PbO film (obtained from the cross-section of the fractured layers) is shown: the bottom of the layer appears denser than middle and the top part [13].

The cross sectional analysis of grown layers reveals that the growth always starts with mostly orthorhombic β -PbO phase forming *seeding layer*. The fraction of β -PbO in the seeding layer is several times that of α -PbO (the properties of α -PbO and β -PbO are

discussed in the Section 2.3.1.). The seeding layer is typically less than few microns thick. After the seeding layer is formed, the composition of the layer changes with further deposition. The fraction of β -PbO drops significantly (about one order of magnitude) and the α -PbO dominates in the bulk part of PbO films.

Degradation of PbO

If PbO layer is exposed to the atmosphere, a significant change in the material composition can occur. In terms of detector performance it results in increase of the dark current, increase in charge trapping and deterioration of transport properties. In case of a short-term exposure (5-10 minutes) the properties of PbO samples were found to recover by placing samples in dry nitrogen atmosphere. However, long term exposure results in irreversible deterioration of PbO performance.

In Figure 2.4 a microscopic view of a cross section of a PbO layer deposited on a glass substrate is shown. The lead oxide film was partly covered with a gold electrode. The border parts of the layer have remained uncovered by the electrode material. After one day of exposure to the air, the sample was broken and the picture of its cross section shown in Figure 2.4 was taken.

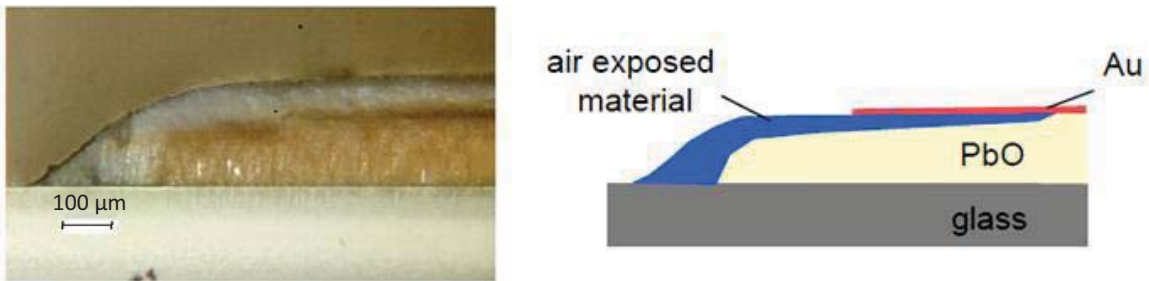


Figure 2.4: On the left: Optical view of the cross section of a PbO layer exposed to air for several days. On the right: Schematic of the cross section features indicating the relevant parts.

Successive inspection after further storage in the air (every time accompanied with the inspection of a freshly broken cross section) reveals a transformation from the original the red/yellow PbO compound (α -PbO / β -PbO) into this white material (Hydro

Cerussite). The transformation has been found to start in the outer (air exposed) regions and continued into the bulk (center part).

2.2: Preparation of PbO layers

Lead oxide samples were produced at the TBRRRI clean room facility by a thermal vacuum evaporation technique. This deposition technique was used because it has three main advantages over other techniques:

- a) It provides higher growth rate than electron gun evaporation [9], sputter deposition [11] and Laser Assisted Deposition (LAD) [12];
- b) The thermal evaporation technique does not require higher substrate temperatures than the acceptable level for a-Silicon electronics used in AMFPI which is the main advantage before the chemical vapor deposition technique (CVD) [10];
- c) The radio frequency (RF) heating method is not feasible because of the high price and huge electrical fields that occur when some kW of RF-energy is present in the vacuum chamber. High electric field implies a high probability to damage the sensitive TFT-arrays [13].

The PbO samples can be grown with a basic evaporation method which has previously been shown to be suitable for development of a human-body size detector [24]. The schematic representation of the evaporation chamber is shown in Figure 2.5. A crucible containing PbO powder of 5N purity is placed inside the furnace and heated by the radiation from a filament. The deposition temperature $\sim 940^{\circ}\text{C}$ at which the evaporation rates are about 1 g/min from the approximately $3 \times 3 \text{ cm}^2$ surface of the liquid PbO. In order to prevent the evaporator from getting damaged as a result of possible crucible breakdown, an outer crucible is used during deposition. The PbO films are grown under small partial pressure of oxygen. Calibrated quartz oscillators are used for monitoring of the growth rate. The quartz crystal is mounted at the side of the vacuum chamber where the mass rate of evaporated material is not too high. This prevents it from getting damaged and makes it possible to keep one quartz crystal over several runs. There is additional heating of the substrate holder through a specially designed Ferro drive. A

good heat transfer between heater and substrate is provided by a Cu plate. As evaporation takes place at a high temperature, a chamber body is externally cooled down. The substrate holder is designed to continuously rotate which is desirable for obtaining layers of uniform thickness. After completing the growth of the layer, the crucible is slowly cooled down to avoid damage due to thermal shock.

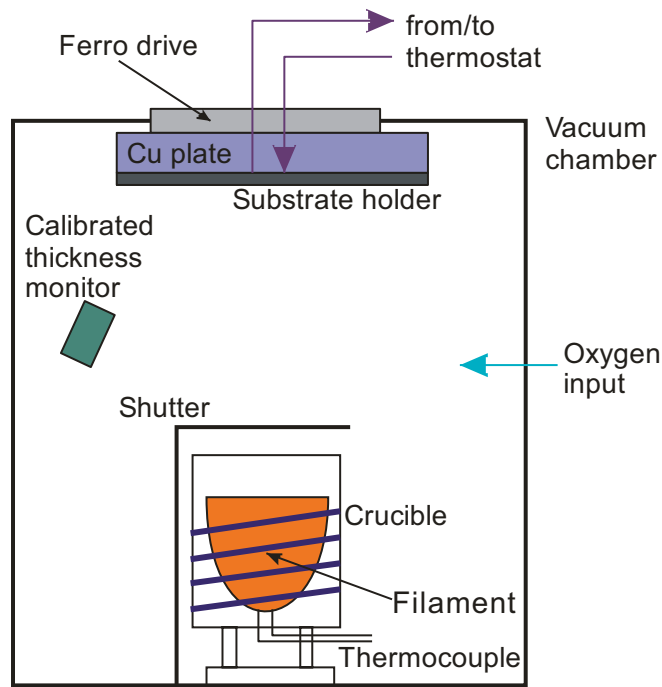


Figure 2.5: Schematic drawing of Lead Oxide vacuum evaporation chamber.

In a typical evaporation run the temperature is increased very slowly ($< 0.2^{\circ}\text{C/s}$) in the range from 400 to 700°C to prevent “eruptions” during initial outgassing of the material. After the melting point of PbO is reached ($T_m = 890^{\circ}\text{C}$) the temperature rate can be increased. However, as temperature approaches the point where evaporation starts T_m in the range of 940 to 955°C the rate of temperature increase has to be reduced again to ensure uniform temperature of all the material inside the crucible. In order to get the desired stoichiometry and composition of lead oxide layers, the evaporation is performed in a pure oxygen environment in the vacuum chamber with a pressure of $4 \cdot 10^{-3}$ mbar which results in a growth rate $\sim 2 \mu\text{m/min}$.

2.3: Raman spectroscopic analysis of the grown layers

2.3.1: Introduction

PbO exists in two polymorphic crystal configurations each with characteristic colour: the tetragonal configuration, α -PbO is red, and an orthorhombic structure, β -PbO is yellow. For imaging applications, red α -PbO is more desirable as its photoconductive properties are much better than the yellow phase β -PbO [18]. However, besides red and yellow PbO there are other lead compounds, e.g., Pb_3O_4 and Hydro-Cerussite which may be present in the grown films. The electro-optical properties of PbO films are directly connected with the composition of the PbO layers and, therefore, it is very important to study the layer composition since it governs the sample performance. The Raman spectroscopy method used in our study is one of the most reliable one in characterization of composition of the grown films [18].

Tetragonal PbO Phase (α -PbO)

α -PbO has a layered crystal structure formed by oxygen atoms sandwiched between lead atoms from both sides. The layers of lead oxide are stacked parallel to the xy plane as shown in Figure 2.6. Such tetragonal arrangement of atoms in lead monoxide is stable at room temperature [16]. The crystal structure of the tetragonal phase is represented by two pairs of oxygen and lead atoms arranged in the lattice according to 129 $P4/nmm$ group symmetry. Each Pb atom is bonded to four oxygen atoms and vice versa, i.e, each oxygen atom is bonded to four lead atoms. The bounds look like a square pyramid with oxygen atoms forming the base. The Raman spectrum of α -PbO as well as its crystal structure is presented in Figure 2.7. There three major peaks on the Raman spectrum, the most intense one has maximum at 145 cm^{-1} and the smaller ones appear at 81 and 337 cm^{-1} [17].

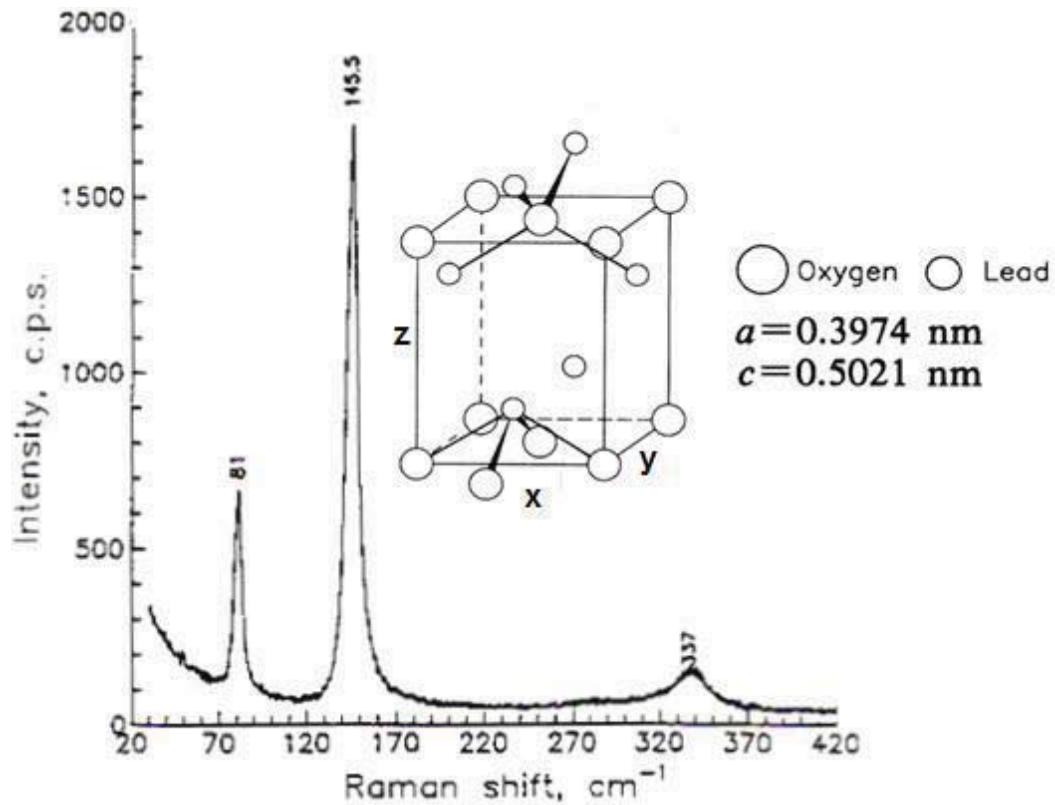


Figure 2.6: Figure shows the Raman spectrum of α -PbO powder and its crystal structure [15, 16].

Orthorhombic PbO Phase (β -PbO)

The orthorhombic β -PbO, has a layered crystal structure similar to the tetragonal phase. β -PbO is metastable at room temperature and becomes thermodynamically stable at the temperatures above 760K [16]. The orthorhombic layers are represented by the zig-zag chains of two pairs of lead and oxygen atoms stacked parallel to the xy plane following D_{3h11} symmetry [16]. The Raman spectrum of β -PbO and its crystal structure are shown in Figure 2.7. As seen in Figure 2.7 for orthorhombic lead oxide the most intense Raman peak appears at 143 cm^{-1} , which is very close to one at 145.5 cm^{-1} seen in α -PbO. Therefore, if the resolution of Raman spectrometer is low, these two peaks merge into a single one making it difficult to recognize the phase. There is another pair of characteristic Raman peaks for α - and β - phases originated at the similar location but they are more separated: 81 and 87.5 cm^{-1} for tetragonal and orthorhombic phases respectively. Due to their low intensity they are also hard to distinguish. However, there is a distinct

peak at 288 cm^{-1} for the tetragonal and at 338 cm^{-1} for orthorhombic PbO which can be clearly differentiated from the Raman spectrum. Therefore, the ratio of intensities of the particular peaks at 288 cm^{-1} for tetragonal and at 338 cm^{-1} for orthorhombic phases can be used to perform the qualitative analysis of the grown films.

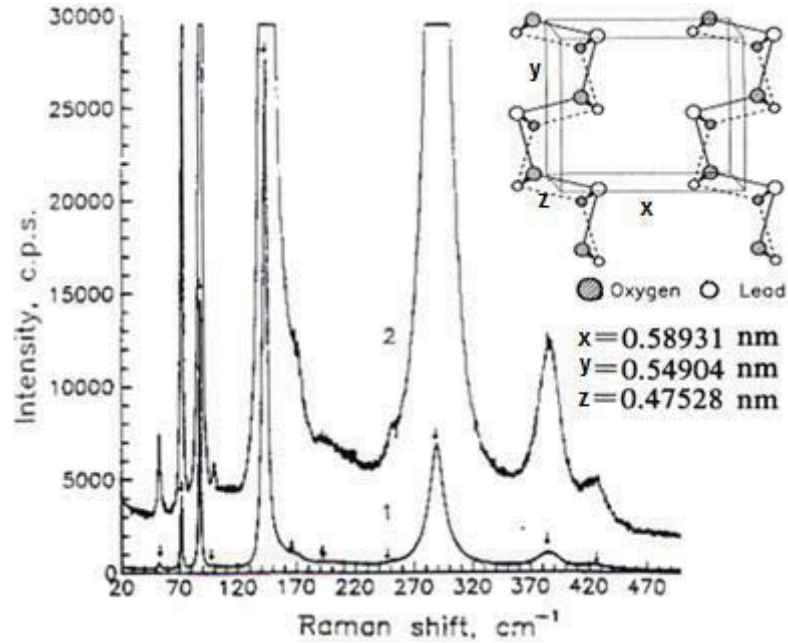


Figure 2.7: Picture shows a Raman spectrum of β -PbO and its crystal structure [15, 16]. Line 2 is the same as line 1 magnified 100 times.

Lead Oxide Pb_3O_4

The Raman spectrum of PbO layers shows that beside tetragonal and orthorhombic phases of PbO, traces of additional lead-oxygen compounds are observed. One of these compounds is Pb_3O_4 also called “red lead” [17]. It is easily distinguished from lead monoxides with Raman spectroscopy due to its well defined characteristic peaks at 122 cm^{-1} and 548 cm^{-1} . The Raman spectrum of red lead is shown in Figure 2.8.

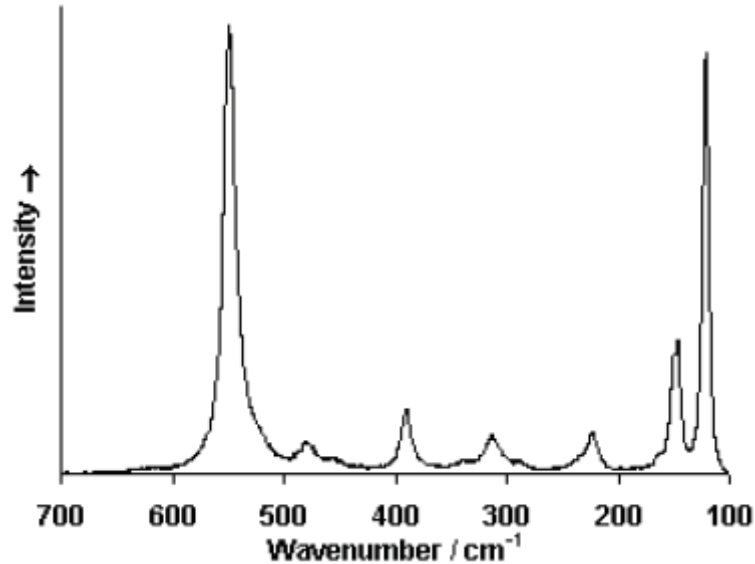


Figure 2.8: Raman spectrum of Pb₃O₄ [19]

Hydro Cerussite

The last compound that is often present on Raman spectrum of PbO layers is Hydro Cerussite (2PbCO₃·Pb(OH)₂). This material is also called a 'white lead', because it appears white in color and for a long time was used as a white pigment in paints. Long term exposure of the evaporated lead oxide material to atmosphere will change it into Hydro Cerussite. The transformation occurs as a result of the reaction between lead oxide with molecules of H₂O and CO₂ present in the atmosphere [17]. Formation of the Hydro Cerussite causes *degradation* of the photoelectrical performance. In order to prevent samples from this kind of degradation, the evaporated PbO layers must be stored in a dry nitrogen atmosphere. This is especially important between the evaporation of the PbO layer and the sputtering of the top electrode, which is needed for application of the external electric field to the sample but plays a protective role for the sample as well.

2.3.2: Results

A composition analysis of PbO layers grown at our facilities has been performed using Raman spectroscopy at Lakehead University instrumentation laboratory. The obtained Raman spectrum of the PbO sample is shown in Figure 2.9.

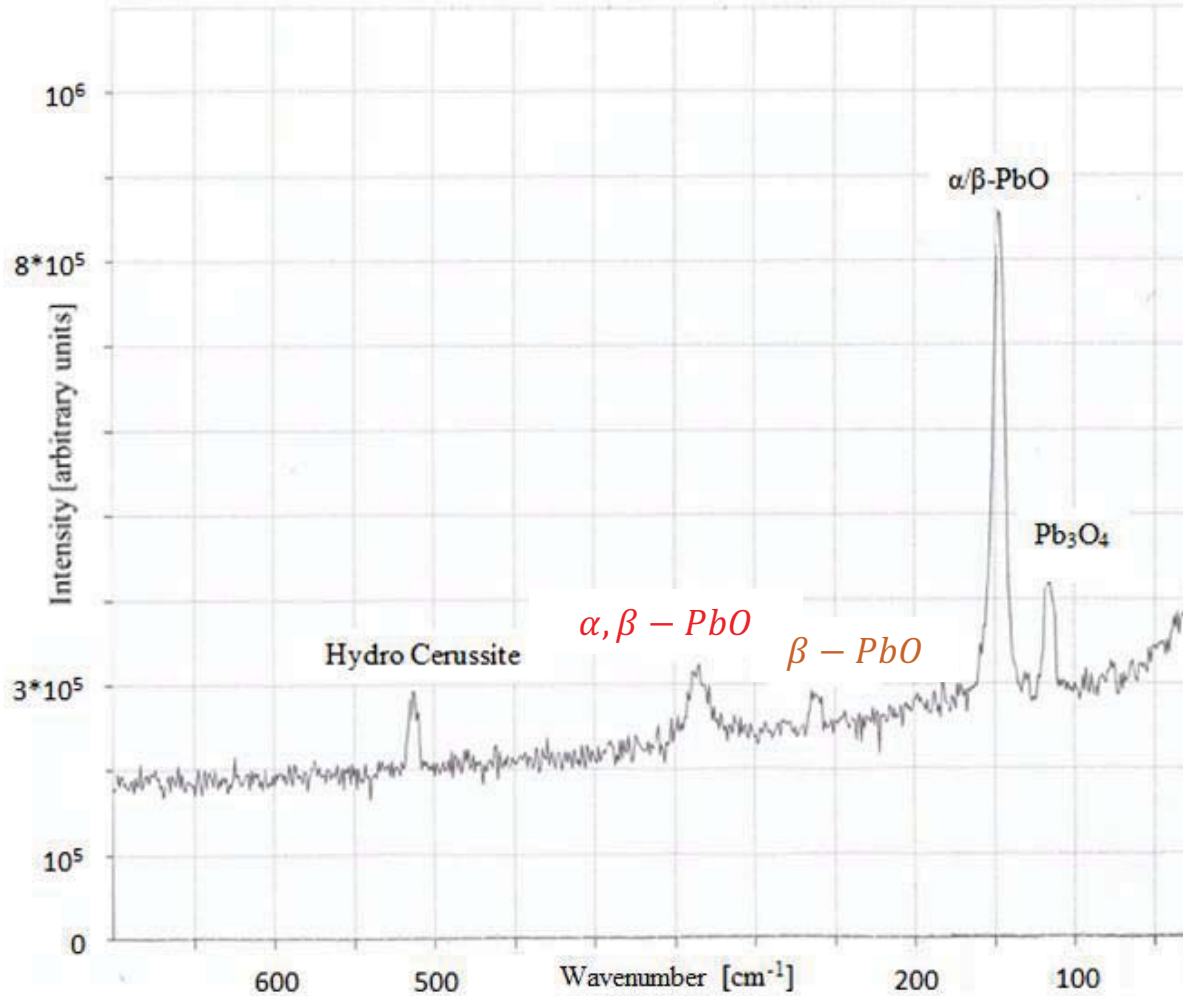


Figure 2.9: Raman spectrum of the surface of PbO film obtained with improved deposition parameters.

As seen in Figure 2.9 the grown PbO film contains high concentration of $\alpha, \beta - \text{PbO}$ as well as other higher oxides of PbO: Hydro Cerrussite and Pb_3O_4 . The Raman peak at $\sim 144 \text{ cm}^{-1}$ is a superposition of two peaks: the $\alpha - \text{PbO}$ at 145.5 and the $\beta - \text{PbO}$ at 143 cm^{-1} that merged together due to low resolution of the Raman spectroscopy system.

2.3.3: Discussion of PbO Raman spectrum

This data reveals that the top layer of the lead oxide film consists mostly of α - and β -PbO, while small fraction of Hydro Cerussite and red lead are also presented. We will now make a more quantitative analysis of the PbO layer composition.

The ratio of Raman peak intensities of β - to α -PbO at 288 cm^{-1} and 338 cm^{-1} respectively, is about $I(288)/I(338)\sim 0.7$, which is remarkably close to the result previously achieved ($\sim 0.5-2$) [17]. This fact means that we achieved a high fraction of α -PbO and a low fraction of β -PbO in our samples and, therefore, the stoichiometry of grown films is improved due to our carefully adjusted deposition parameters.

In summary the ratio of β -to α -PbO varies during the growth, but in general the bulk layer is composed mostly out of α -PbO and the seeding layer of β -PbO [18]. In order to make the evaporation process fast and cost-effective the deposition rate is desired to be as high as possible. It was found that above a certain threshold rate, further increase in deposition rate causes a rapid increase in β -PbO. The domination of the β -PbO in the seeding layer as well as its dependence on deposition speed can be explained by its higher nucleation rate in comparison to the α -PbO [18].

2.4: Conclusion

The experiments on PbO deposition show that the best film composition is obtained at growth rate maintained at 1.3 $\mu\text{m}/\text{min}$ and an oxygen pressure of about 1.3 mbar. This result is consistent with the previously published data [24]. However, with our optimized deposition parameters, the Raman spectroscopy of grown layers shows low β - to α -PbO ratio meaning good layer composition comparable to the best achieved previously. The photoconductive performance of grown layers was validated with a number of different techniques and will be discussed in the next chapter.

So far, the samples were constantly stored under a continuous flow of dry nitrogen in order to prevent transformation of PbO into Hydro Cerrussite. Part of our future work will address the problem of permanent degradation by devising a protective layer that will prevent atmospheric damage without affecting the photoconductive performance.

Chapter 3: PbO X-ray detector for fluoroscopic applications

3.1: Introduction

The basic electronic parameters of PbO charge mobility, X-ray-to charge conversion efficiency and dark current need to be known in order to evaluate its suitability for medical imaging applications. This chapter is dedicated to estimating the temporal performance of PbO, its charge yield and dark current. The response of PbO to different X-ray pulse durations (70 ns, 50 ms and 5 s) was successfully utilized to investigate transport and charge collection in polycrystalline PbO. The contribution of each type of carriers to the X-ray induced current can be separated based on the mobility difference, so that electron and hole transport can be distinguished. From the waveform of transient current flowing in the sample, we were able to estimate the transit mobility ranges for charge carriers. The measurements were performed at different temperatures to check its influence on transit time. Also, knowledge of transit time allowed us to measure the quantum efficiency of PbO in terms of average energy required for the production of a single electron-hole pair (W_{\pm}). For this purpose the X-ray induced photocurrent and Pulse Height Spectroscopy methods were utilized. In initial experiments the charge in the PbO sample was generated by a broad spectrum of X-ray energies whereas PHS method is based on measurement of charge produced by monoenergetic X-ray photons of a specific energy. Finally the dark current-voltage dependence of PbO film was measured. This is one of the most important characteristics of a photoconductor as the shot noise intrinsic to it degrades the dynamic performance of the detector. The dark current has a complex nature and can be accounted by several phenomena namely contact injection and bulk thermal generation. The data obtained from the above experiments is required for both determinations of basic parameters of PbO that were not firmly established prior to this work as well as to evaluate PbO as an X-ray-to-charge transducer for applications in medical imaging direct conversion detectors.

3.2 Background: fundamentals of Plumbicon operation

PbO has a long history of application. In the early 60's it was already successfully utilized for optical imaging as a photosensitive target in the Plumbicon – a kind of video camera tube. This type of vacuum target was dominant TV broadcasting tube for 30 years and only in the last 15 years was replaced by CCD and CMOS sensors. Plumbicon video tubes utilized a thin ($\sim 20 \mu\text{m}$) layer of tetragonal PbO deposited upon a transparent tin oxide (SnO_2) electrode. This electrode was typically biased at $\sim 40 \text{ V}$ positive with respect to the back *free surface* of PbO i.e. a surface without electrodes, but with surface traps on which a latent charge image can form. The scanning electron beam was used to bring the free surface to cathode potential in order to discharge the free surface of lead oxide, and in the process to reestablish the 40 V drop across the PbO layer. When light hits the front side (electrode) of the phototarget, the photocarriers are generated in proportion to the incident light intensity (see Figure 3.1). The electrons are almost immediately swept out by the applied field to tin oxide electrode and do not contribute to the current flowing in the external circuit. Holes travel along the lines of electric field towards the negatively charged free surface of PbO. When scanned, the electron beam completes the external circuit so that the current recharging the free surface is measured and becomes the signal which can be displayed directly on a monitor or digitized and stored.

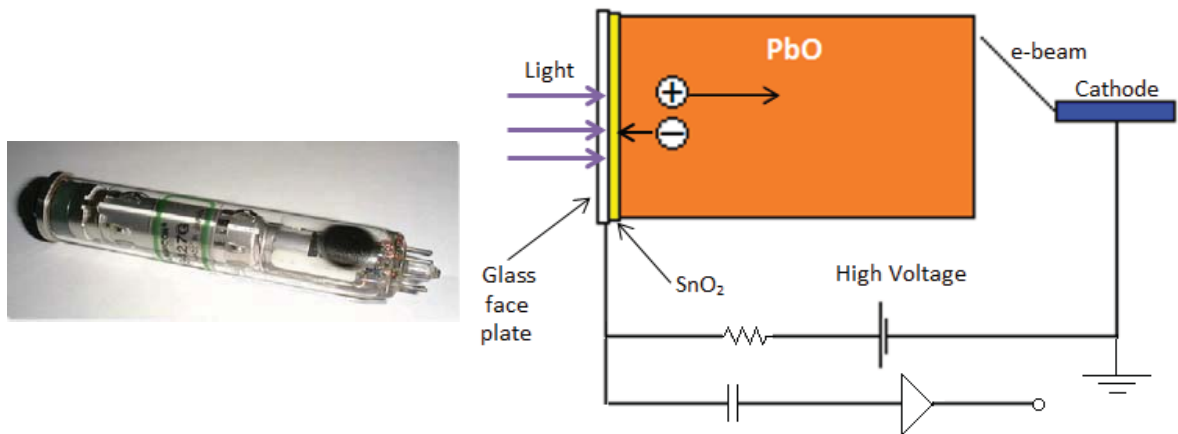


Figure 3.1: Left: A Plumbicon tube used for TV broadcasting [30]. Right: A schematic representation of Plumbicon operation in the normal mode.

The fundamental feature of Plumbicon from vidicons was the intrinsic *p-i-n* junction nature of the PbO layer. The *n*-region was formed on the PbO-SnO₂ interface and the *p*-type layer was formed on the electron beam side. However, the bulk PbO layer behaves as an intrinsic semiconductor. The interfaces (PbO-SnO₂ and *p*-type layer) act as blocking electrodes suppressing injection. The structure was reverse biased so that the dark current was limited to a relatively small value.

Plumbicons were very successful for optical applications, but they utilize a relatively thin layer of PbO and employ electron beam readout [29]. They are now essentially obsolete having been replaced by much more compact and energy efficient solid state silicon sensors (e.g. CCDs and CMOS). For medical imaging applications, the electron beam has to be replaced by a two-dimensional array of pixel electrodes [30] or XLV system and a relatively thick layer of photoconductor is required for good X-ray absorption.

3.3: Methods and materials

3.3.1: PbO with metal electrodes

The adjusted thermal vacuum evaporation technique described in the previous chapter was used to deposit 42 μm thick and 12.5 mm in diameter PbO samples on the 25x25 mm² glass substrate, covered with transparent conductive Indium Tin Oxide (ITO) coating which serves as a bottom electrode. Subsequently the other electrode, a gold contact 2 mm in diameter, was sputtered in the clean room area as a top electrode (see Figure 3.2). The metal top contact replaced the electron beam as a bias electrode. Due to the very porous structure of lead oxide, a relatively thick layer of Au (300 nm) is needed in order to provide uniform contact. The ITO-PbO-Au structure allowed an application of external electric field for the characterization of the sample's response to the incident radiation and for measurement of other characteristic parameters.

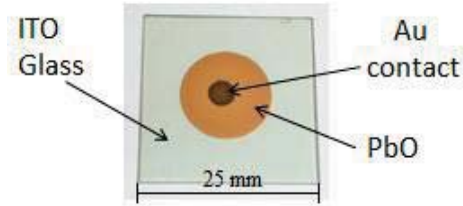


Figure 3.2: The PbO sample with a gold top electrode.

3.3.2: Electrical model of experimental apparatus

To model the electrical behavior of the PbO detector under constant bias the PSpice program was used. This software allows to simulate the behavior of PbO from the electrical circuit point of view. Under a fixed applied electric field the PbO sample with DC power supply and oscilloscope was modeled as shown in Figure 3.3 and now we will discuss the function of the circuit components.

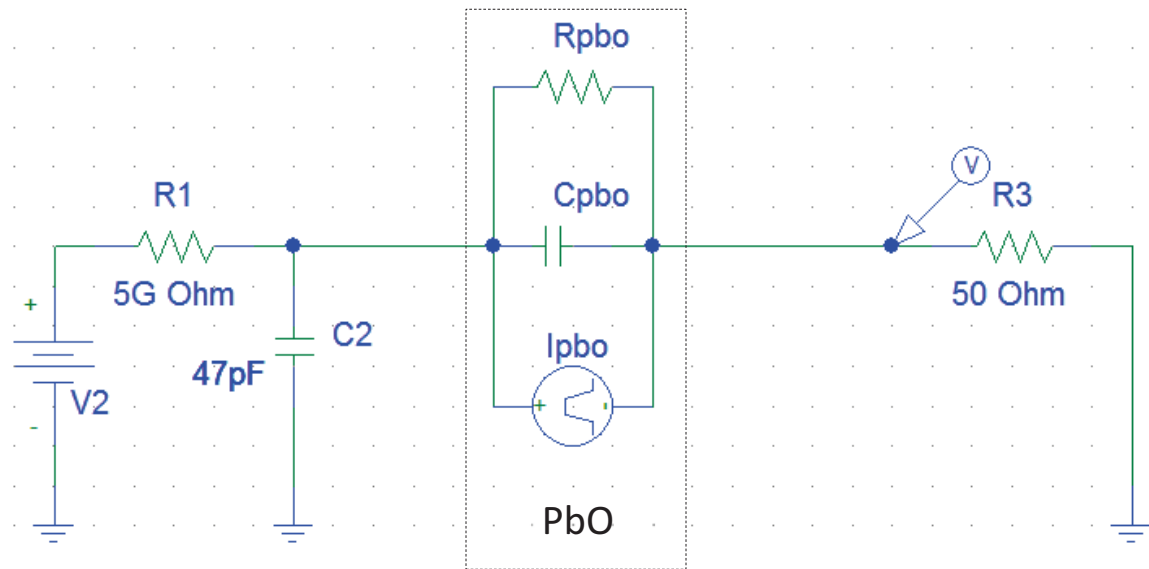


Figure 3.3. Electrical model of the PbO connected to the high voltage power supply and 50 Ohm oscilloscope input. The PbO sample is shown as a current source connected in parallel with resistor and capacitor.

The response of detector to an X-ray pulse can be represented as an ideal current pulse source with a resistor and capacitance connected in parallel as shown in Figure 3.3. The resistor R_{PbO} accounts for the dark current. Its value is not constant but depends

on the applied electric field to the PbO layer. The value of R_{PbO} was calculated separately for different voltages by measuring dark current and determined to be about 100G Ohms at $V_{bias}=10$ V/ μ m. The capacitance of the sample was calculated assuming that behaves as a parallel plate capacitor, which is a reasonable assumption since the size of the contact was much larger than the sample thickness. In this case the sample capacitance is:

$$C_{PbO} = \epsilon_{PbO} \epsilon_0 \frac{A}{d} \quad (3.1)$$

where ϵ_{PbO} is the relative dielectric constant of the porous PbO, ϵ_0 is the electric permittivity of the vacuum, A is the contact area, d is the thickness of PbO film (42 μ m). From samples to samples the ϵ_{PbO} changes a little due to variation of film density. In this regard, the detector capacitance was measured separately for each sample with a help of LCR meter MCP model BR 2822. The measured value was found to be 4 pF that corresponds to dielectric constant $\epsilon_{PbO}=15$, which is about half of the dielectric constant of crystalline PbO [31]. This value may be justified by the fact that density of the film is about half of the PbO powder density.

The 50 Ohm resistor is introduced to account for the input resistance of the oscilloscope 300MHz Tektronix model TDS-3034B. Resistor R_I of magnitude 5 G Ohm is used as a protective resistor in order to prevent damage of the oscilloscope in case of electrical breakdown of the PbO sample. Capacitor C_2 provides the signal ground and also in combination with resistor R_I helps to filter out any noise coming from the power supply V_2 .

When the PbO detector is irradiated with the pulse of X-rays under applied electric field it responds with a pulse of electric current. The duration of X-ray pulse as well as response of lead oxide is very short in comparison to the RC constant of the detector, so the resistance of the PbO can be ignored and we can consider only the capacitances present in the circuit.

The value of C_2 was calculated to provide complete charge collection without deterioration of the waveform of the signal observed on the scope. The impedance offered by a capacitor C_2 is much smaller than the path through the resistor the R_I , so

practically all signal current flows through the capacitor while all DC current flows through the resistor.

The efficiency of the circuit in collecting the charge generated by the PbO in response to the X-ray pulse is given by the relation:

$$\eta = \frac{C_2}{C_2 + C_{PbO}} \quad (3.2)$$

In practice, the capacitance C_2 is much higher than C_{PbO} , so the ratio is close to unity. The charge collected on the capacitors eventually discharges through the resistances of the circuit.

In the absence of irradiation all capacitances present in the circuit shown in Figure 3.3 may be ignored and under applied external electric field only the dark current of PbO I_{dark} flows in the circuit. Since the protection resistor R_I is connected in series to the lead oxide sample, the actual bias applied to the detector is reduced by a small amount ΔV that drops on resistor R_I :

$$\Delta V = I_{dark} R_P \quad (3.3)$$

For the 100 pA of dark current the voltage drop across the protective resistor is very small (0.5 V) and can be neglected. The voltage drop on the 50 Ohm input of the oscilloscope is much smaller, so may also be safely neglected.

3.4: X-ray response

The response of PbO on a very short X-ray excitation has been demonstrated to be a very useful technique for measurement of transport processes in lead oxide under X-ray excitation [23]. When the detector is exposed to radiation, electrons and holes are generated across sample thickness rather than just near the surface. The X-rays are generated with a mean X-ray energy of 30 keV and in PbO are characterized by a long attenuation length D (inverse of the linear attenuation coefficient). For Lead Oxide, the

attenuation length is 75 μm , and 5 mm for the glass substrate. We can assume thus that X-ray absorption is uniform across the 42 μm thick PbO sample.

3.4.1: Experimental apparatus

The experimental apparatus used for X-ray response is shown in Figure 3.4. The PbO samples were irradiated from the ITO side with short (70 ns) X-ray pulses. A wide range of electric fields in the range 2 to 20 V/ μm were applied, which are considerably higher than the maximum bias applied in prior experiments [24]. The positive bias polarity was applied to the ITO side during all experiments. Such polarity was chosen as the one that provides the lower levels of dark current and will be discussed later. The maximal applicable field was restricted by the increasing dark current. The transient current flowing in the sample under X-ray exposure was observed by the 50 Ohm oscilloscope.

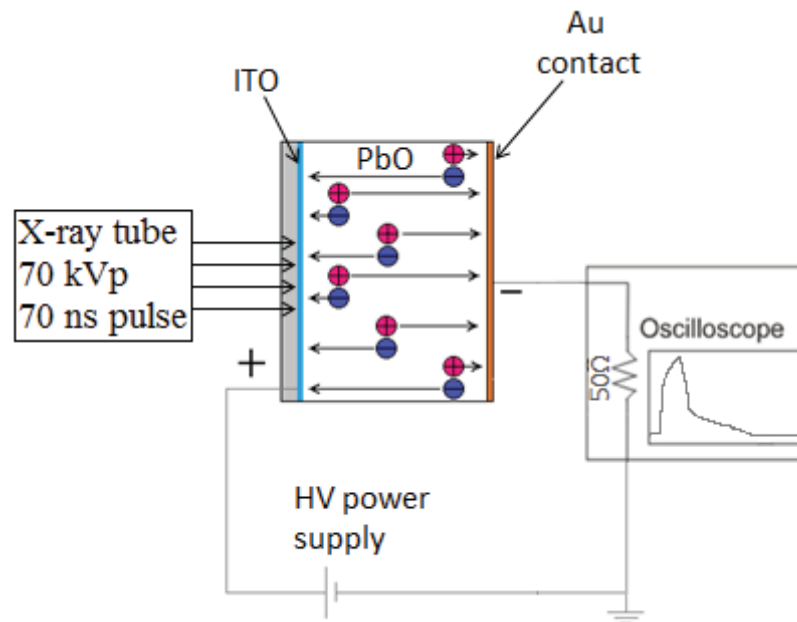


Figure 3.4. The experimental X-ray response apparatus is shown.

3.4.2: Results

The X-ray pulse was produced by a Golden Engineering XR 200 portable X-ray generator. This generator provided such an X-ray spectrum that a roughly uniform

absorption is obtained throughout the PbO sample resulting in almost uniform generation of charge carriers. The bias potential V , applied across the thickness L of the PbO layer, establishes uniform electric field $E_{PbO}=V/L$. The drift of electrons to positive and holes to negative electrodes induces a current i_{PbO} in the external circuit resulting in the X-ray response waveform. The waveform observed on the oscilloscope reflects the transit of both types of carriers (electrons and holes). Figure 3.5 shows the normalized X-ray response of PbO layer biased at $3\text{ V}/\mu\text{m}$ as well as of a-Se biased at $60\text{ V}/\mu\text{m}$ and silicon photodiode that were used for comparison. From the response of all the detectors it is seen that instead of producing a single X-ray pulse, the XR 200 produces a second pulse right after first one.

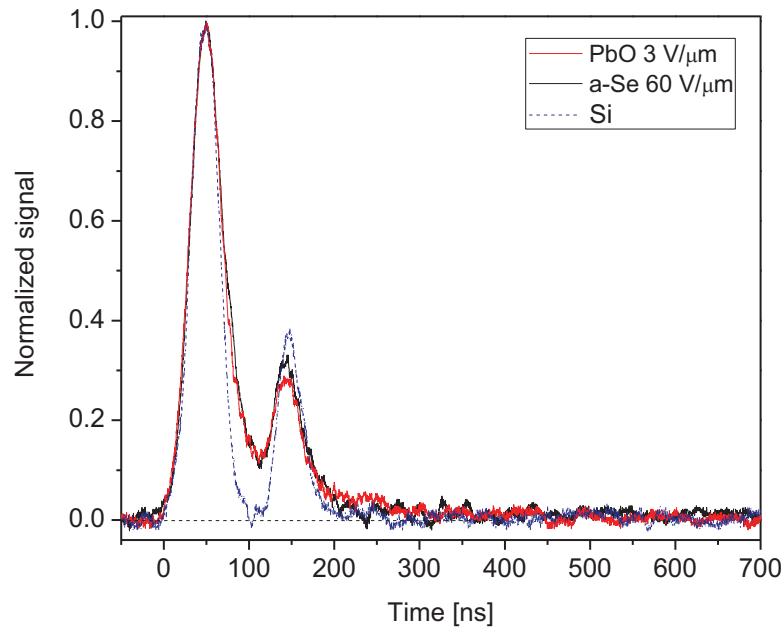


Figure 3.5: Comparison of detector performance of PbO, a-Se and Si-photodiode.

An X-ray response of PbO for different fields applied to the sample shown in Figure 3.6 reveals that even at $3\text{ V}/\mu\text{m}$ the majority of generated charge is seen to be collected in less than 500 ns . The obtained waveforms shows that response of PbO follows the X-ray pulse, however there is a *tail* present at the end of exposure of duration $\sim 100\text{ ns}$.

The examination of the temporal behavior of the PbO as a function of temperature was performed to investigate the influence of temperature on the transport properties of lead oxide and shown in Figure 3.7.

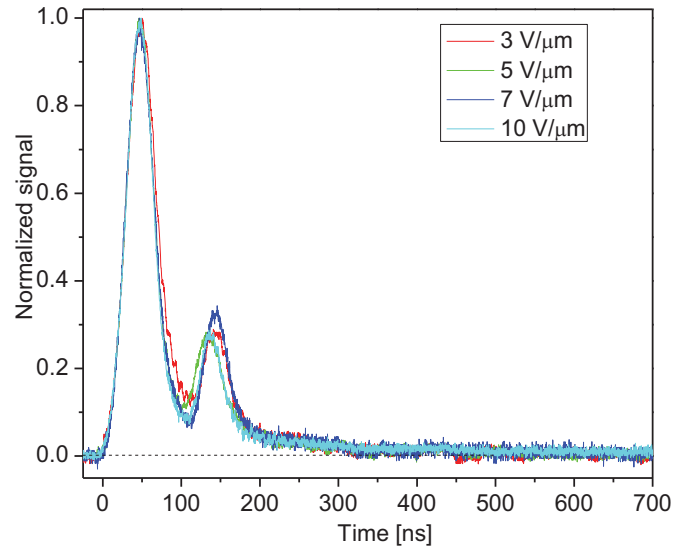


Figure 3.6: Normalized X-ray response from PbO for different electric field is shown.

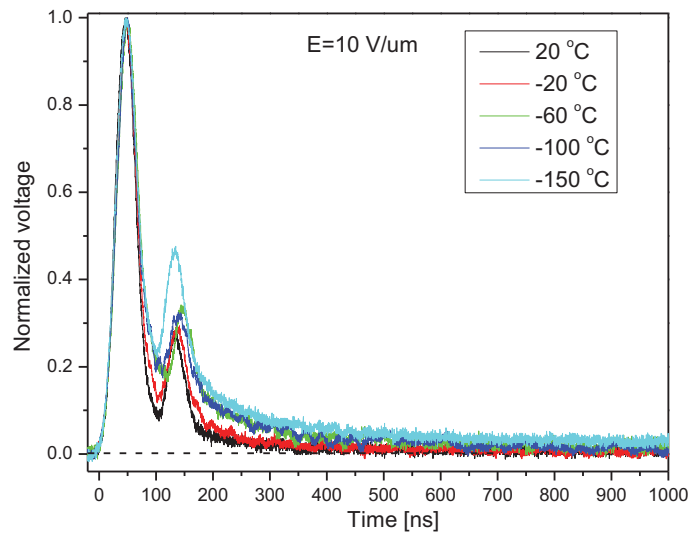


Figure 3.7: The dependence of transit time on temperature is shown. The decrease of temperature leads to a larger and more prominent tail.

3.4.3: Discussion

From the X-ray response of Si photodiode shown in Figure 3.5 we can see a double pulse produced by generator. The fact that we can clearly resolve two peaks with PbO indicates that the X-ray pulse duration is longer than the transit time of the fast carriers in lead oxide. This only allows us to put a lower limit to the mobility of electrons. However, the signal between and after the X-ray pulses does not immediately drop to zero indicating the presence of slower carriers. The similar response was produced by a-Se which already gone into industrial production, however suffers from low charge yield and high operating electric field [52]. Also, comparing with response of Si photodiode, it is seen that the X-ray response of PbO has some trapping.

Assume that the transit time of fast carriers (electrons) T_e is as low as the X-ray pulse duration (70 ns), for 42 μm thick layer of PbO at 3 V/ μm , the lower limit of mobility for electrons can be calculated according to the following relation [23]:

$$\mu_e = \frac{L_{PbO}}{E * T_e} = 1.4 \frac{cm^2}{Vs} \quad (3.4)$$

where L_{PbO} is the sample thickness and E is applied electric field.

From the plots above it is seen that 500 ns after the end of exposure, there is no significant charge left in PbO. If we take 500 ns as the transit time of slow carriers (holes) T_h than the mobility of holes is

$$\mu_h = \frac{L_{PbO}}{E * T_h} = 0.28 \frac{cm^2}{Vs} \quad (3.5)$$

For the same electric field the mobility of electrons is found to be at least five times higher than the mobility of holes. These are the first experimental results revealing the mobility parameters in polycrystalline lead oxide.

As seen from the temperature experiments shown in Figure 3.7 the release trapping of slower carriers becomes more and more pronounced with decrease of temperature. The tail at the end of exposure increases in magnitude, but drops to zero within a few μs . However, holes are seen to be trapped more, the behavior of electrons is shown to be

unaffected by temperature decrease. Two separate X-ray pulses may still be clearly distinguished even at -150 °C. This indicates that the transit time of electrons must be much shorter than the X-ray pulse duration.

3.4.4: Conclusion

The temporal response of PbO to a 70 ns pulse was investigated and compared with the response of other detectors (a-Se and Si photodiode). The experimental results indicate high mobility of charge carriers, comparable to amorphous selenium. The duration of the X-ray pulse was relatively too long for estimating the mobility of electrons and accurate determination of holes mobility was limited by the presence of the second pulse during the X-ray exposure. However, as seen from the results, the majority of carriers are swept out of the sample during less than half a microsecond for 3 V/ μm applied field, which satisfies the temporal requirements of fluoroscopic imaging. The mobility of electrons is shown to be at least five times higher than for holes. The X-ray response measurements at low temperatures indicate that mobility of electrons may be even higher than $1.4 \frac{\text{cm}^2}{\text{Vs}}$, as two separate pulses can be clearly distinguished at -150 °C. The relatively long tail was more noticeable at lower temperatures indicating an enhanced trapping of slow holes. Another possibility is that only one type of carriers (electrons) was seen and holes are orders of magnitude slower and experience deep trapping. In this case signal waveform shows fast motion and small trapping (~10%) of electrons, whereas slow motion of holes is not visible on ns scale. More experiments for different integration times were performed in order to clarify this issue and provide a quantitative characterization of X-ray induced photogeneration in lead oxide.

3.5: Measurement of X-ray photogeneration in polycrystalline PbO

As there is no firmly established data on electron-hole formation energy in PbO so there is some ambiguity in W_{\pm} . This value has been measured previously to be within the window 5-20 eV/ehp, whereas for other polycrystalline candidates to be used for X-ray-to charge direct conversion, those values are known more accurately [33]. The theoretically predicted value of W_{\pm} in lead oxide according to Klein's rule is 5.73 eV/ehp

[24], however experimental values are generally higher. Previous experimental measurements of charge yield (Y) show a strong dependence on applied field E , which is a typical behavior for many photoconductors [24, 35]. The relatively higher than theoretical values of W_{\pm} (≈ 10 eV/ehp at 3.5 V/ μm [24]) and dependence of charge yield on applied field indicates that a fraction of X-ray generated charge undergoes trapping (deep traps) or recombination and thus does not contribute to the signal. However, under constant exposure with increase of electric field the charge yield grows, which means that the portion of trapped/recombined charge decreases with increase in applied field. Such behavior is explained by the fact that with increase of applied electric field the average distance traveled by a charge carrier before trapping or recombination (known as schubweg) also increases. This value is related to the applied bias as follows:

$$s = \mu\tau E \quad (3.6)$$

where μ is the carrier mobility, τ is the carrier lifetime and E is the field applied to the PbO layer. For efficient charge collection and good temporal response of the detector, the schubweg should ideally be several times greater than the thickness of the photoconductor, which is usually about $200 \mu\text{m}$ [4].

Previous measurements of W_{\pm} in PbO utilized the X-ray induced photocurrent method [36], where the total generated charge was integrated over the X-ray pulse duration and compared with the energy of the incident flux of radiation. The presence of a residual signal after the end of exposure and its unknown nature makes it impossible to define the integration times precisely. In addition the accuracy of the method is affected by the necessity to accurately know the spectrum of the incident radiation. These experiments were not straightforward and test samples were prepared with different deposition techniques [24, 35]. In these experiments the saturation point of the charge integration was not reached, since the maximum applied field E was only $3\text{-}3.5$ V/ μm [24, 35]. Further increase of bias resulted in extraordinarily high dark current. Therefore the value of W_{\pm} is not known as accurately as is necessary to design a practical X-ray detector and we will now outline the methods we have utilized to overcome the problems encountered by previous investigators and establish W_{\pm} for PbO more accurately.

3.5.1: X-ray induced photocurrent method

3.5.1.1: Experimental apparatus for X-ray photocurrent method

In order to compare our results with those found in the literature, we utilized an apparatus for X-ray photogeneration current measurement shown in Figure 3.8. A standard medical X-ray tube provided X-rays pulse of the desired duration. The ionization chamber Keithley model 96035 was used in order to measure the X-ray exposure, and a 21 mm thick slab of aluminum was used in order to mimic the attenuation in the human body and also to limit the range of energies incident on the detector. An external high voltage power supply maintained the desired voltage drop across the sample and the signal current induced by the X-ray pulse in PbO layers was observed on the 150MHz digital oscilloscope Tektronix model TDS 420.

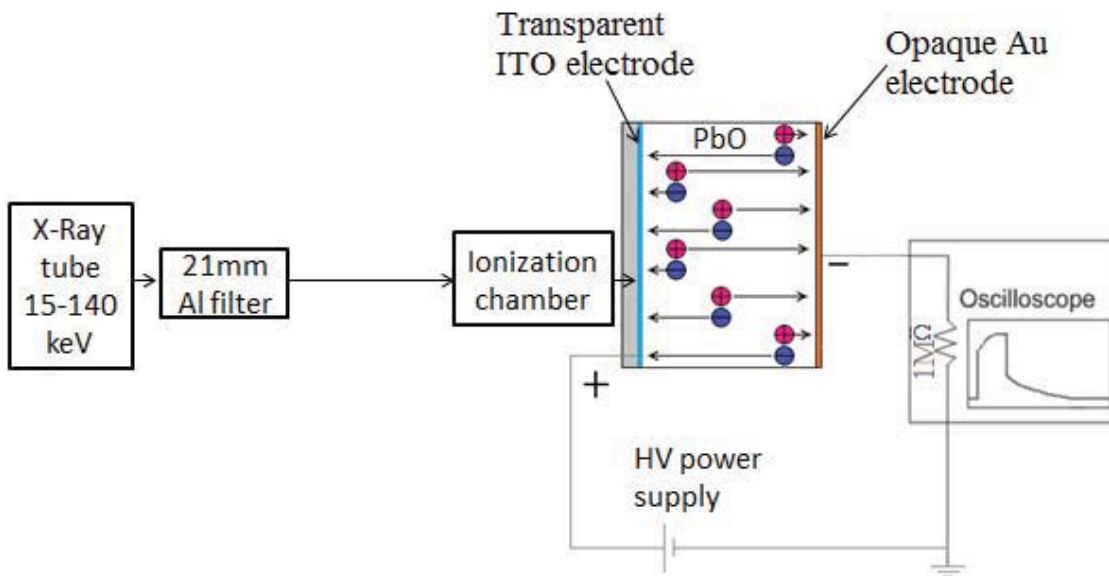
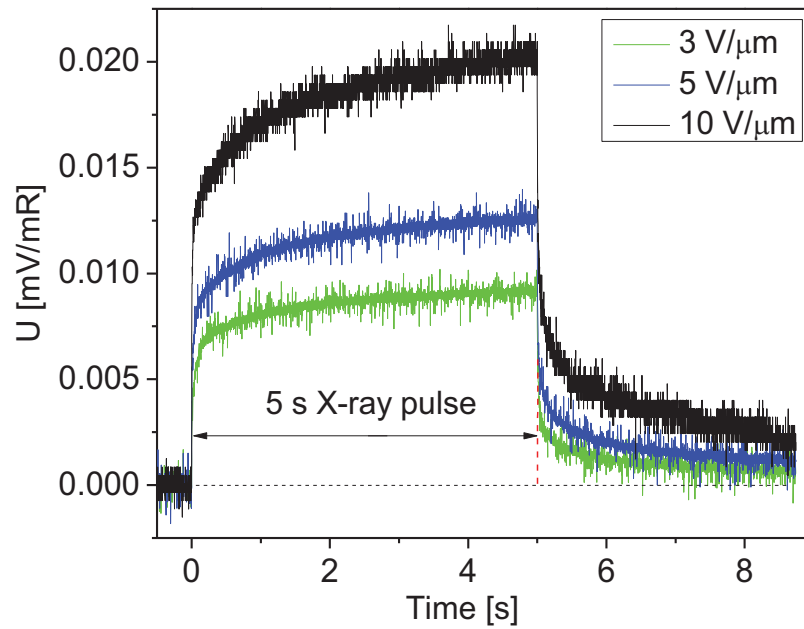


Figure 3.8: Schematic diagram of the schematic apparatus for measurement of the X-ray induced current.

3.5.1.2: Results

The X-ray responses of the PbO specimen for different electric fields are shown in Figure 3.9. The waveforms were taken at 70kVp spectrum and normalized to exposure.

As seen the amplitude of the signal grows during the X-ray pulse and does not drop down to a base line immediately at the end of exposure. The fluctuations seen on the waveform taken during 50 ms exposure are due to fluctuations in X-ray machine itself. They are also present during 5 s X-ray exposure, but cannot be resolved on this scale.



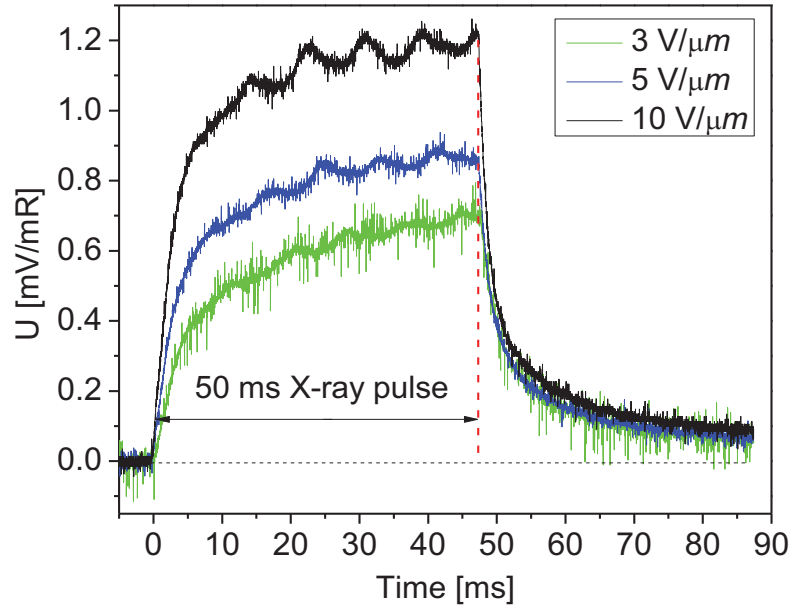


Figure 3.9: Top: Response of PbO to a 5 s X-ray pulse showing an increase of residual signal with increase of applied field. Bottom: The response of PbO on the 50 ms X-ray pulse for several electric fields is shown. The tail is independent on E .

3.5.1.3: Discussion

Under irradiation of PbO with a 5 s pulse of X-rays the signal amplitude grows, with increase in applied field. In addition, a residual signal that disappears with time is observed at the end of X-ray pulse. The magnitude of the residual signal is about 10 % of the maximum value 1 s after the end of exposure and decays to less than 1 % in 10 seconds. However, if the time of X-ray irradiation is decreased to 50 ms only, the amplitude of the signal keeps growing with increase of applied field, while the amplitude of the residual signal does not depend on the field. The collected charge was calculated as the area under the current waveform during exposure time according to the formula:

$$Q_{total} = \int_0^{T_{pulse}} I_{PbO} dt \quad (3.7)$$

The value of W_{\pm} is plotted in Figure 3.10. It was obtained as a ratio of the total collected charge within pulse duration to the total energy of the X-ray flux that was calculated from the measured X-ray exposure.

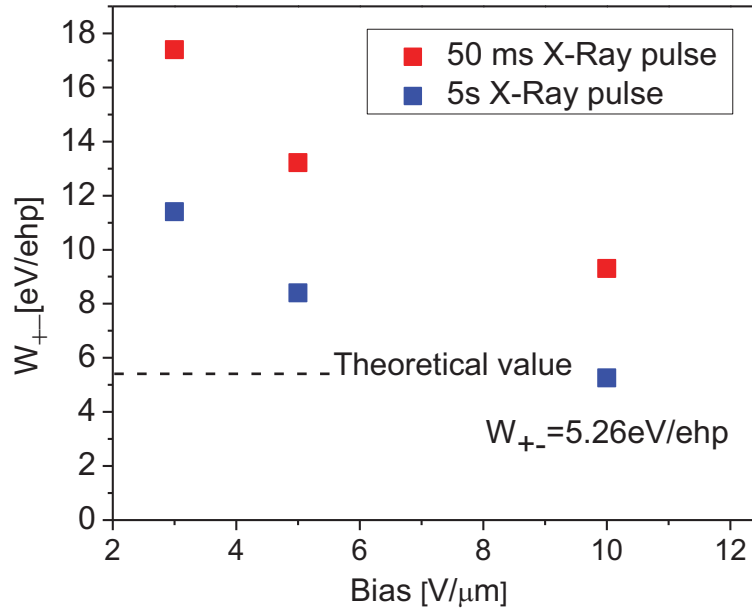


Figure 3.10: The W_{\pm} is plotted versus applied electric field for different pulse durations. Uncertainties are smaller than the size of the plotted points.

As shown on the Figure 3.14 the value of W_{\pm} decreases with electric field. It approaches to the theoretical value, the value of W_{\pm} measured at 10 V/μm and 5 s X-ray pulse ($W_{\pm}=5.23$ eV/ehp) possibly exceeds the theoretically predicted value (~6 eV/ehp). Also W_{\pm} is about half for 50 ms exposure in comparison with the one obtained at 5 s radiation pulse. A possible explanation of this phenomenon is the presence of injection current from the electrodes, so the longer the exposure the larger contribution of the injected current and the lower W_{\pm} . However, a decrease of W_{\pm} with X-ray pulse also might mean that there are some deep traps present in the materials and it takes more than 50 ms to collect all carriers. The fact that at 10 V/μm and 5 s X-ray pulse W_{\pm} is possibly lower than theoretical limit could indicate that there is a contribution of injected current, but for values of W_{\pm} higher than theoretically predicted value it is hard to distinguish

between charge injection and detrapping process. A blocking structure (which limits the injection) is needed to verify this hypothesis.

The values of W_{\pm} were also verified with the Pulse-Height-Spectroscopy (PHS) method discussed next.

3.5.2: The Pulsed Height Spectroscopy method

Pulse height spectroscopy (PHS) performed with a monoenergetic source of X-ray photons was shown to be a more accurate way of determination of electron-hole pair creation energy [36]. An advantage of the PHS method is that the position of the spectral peak is relatively insensitive to dark current. The dependence of W_{\pm} on applied bias was measured using radioactive sources instead of the X-ray generator. Radioactive sources generate well known monoenergetic spectral lines therefore eliminating errors due to the imperfect knowledge of the X-ray spectrum. The main idea behind PHS is to irradiate the detector with monoenergetic X-rays of low enough intensity that the charge generated by each x-ray photon interaction can be separately detected and processed. From the accumulation of many interactions a histogram of the charge is then created. The histogram represents the pulse-height-spectrum as a number of counts for a given amount of charge generated and generally shows a peak for each X-ray energy. The peak position represents the mean charge generated for that energy. The width of the spectrum is due to a combination of all noise sources associated with the apparatus and the detector itself and intrinsic spectral width of the radioactive source.

3.5.2.1: Experimental apparatus to measure PHS

The experimental apparatus for characterization of PbO using a PHS spectrometer is shown in Figure 3.11. A 42 μm thick layer of PbO was used as the radiation detector. An external electric field was applied through the bias electrodes in order to create a voltage drop across the sample. The signal generated by each X-ray photon was readout from the top contact coupled to the a noise charge preamplifier, then to the pulse shaping amplifier (Ortec model 673) and then to the multi-channel analyzer (MCA, Ortec model ASPEC927).

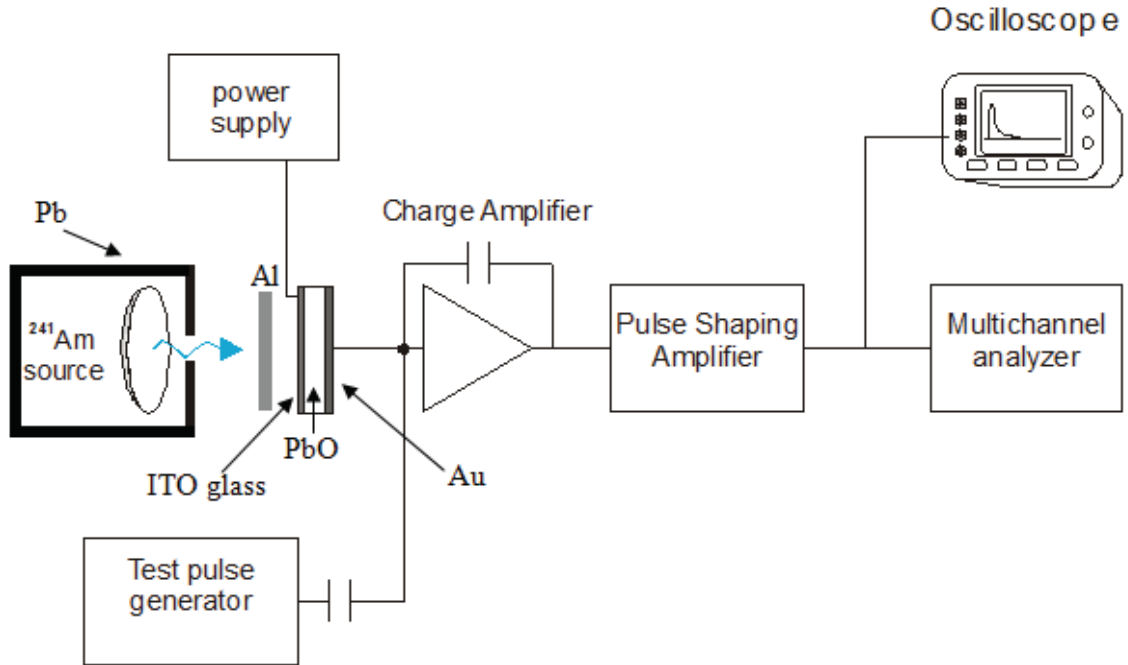


Fig. 3.11: A schematic representation of the PbO-based spectrometer is shown. A radioactive source ^{241}Am was used as monoenergetic source within a lead collimator. 1.5 mm of Al was used to minimize the influence of low-energy X-rays emerging from the source. The signal generated in PbO in response to X-ray absorption is processed by the charge and pulse shaping amplifiers and finally by the multichannel analyzer.

For an accurate measurement of EHP formation energy with the PHS method, the shaping time must be properly selected. As there were no reliable data available on PbO carrier mobility in the literature, the shaping time was selected basing on our previous short (70 ns) X-ray response experiment. As seen in Figure 3.12, the total transit time is less than $1\ \mu\text{s}$ at lowest applied field $3\ \text{V}/\mu\text{m}$ and decreases with increase of applied voltage and the shaping time was chosen to be $\tau_{shaping}=20\ \mu\text{s}$.

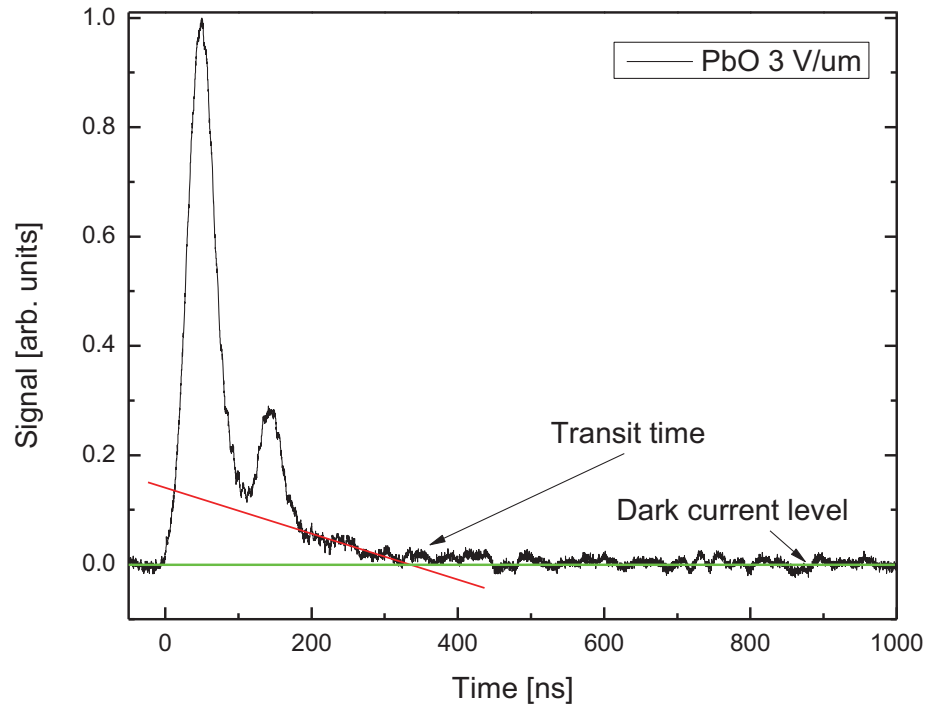


Figure 3.12. Response of PbO to a 70 ns X-ray pulse.

The PbO samples were kept under continuous flow of dry nitrogen during the entire experiment. The measured dark current was very low. At an electric field of $10 \text{ V}/\mu\text{m}$ the dark current was $I_{\text{dark}} \sim 300 \text{ pA}/\text{mm}^2$. Vibration isolation was used in order to eliminate the influence of external vibrations on the measured results. Prior to the electrical measurements, the PbO samples were rested for several days in complete darkness in order to dissipate any leftover trapped charge from previous experiments. The measurements were repeated several times with the same experimental parameters (electric field and photon energy, shaping time) to verify the repeatability of results. The obtained values of W_{\pm} only slightly differed within $\pm 0.5\%$ of measurement accuracy. Current pulses and spectral peaks due to radiation absorption could be clearly distinguished from the background noise. An ^{241}Am source was used to generate 59.5 keV monoenergetic radiation. Other decay modes of this material were not of interest for our research and were small enough to not affect the results. At characteristic radiation $\epsilon = 59.5 \text{ keV}$ the probability of photoelectric interactions is 89.1%, meaning that the

spectral lines represent full absorption of the incident photon energy. The main sources of X-ray noise are Compton backscattering due to the glass substrate, aluminum box and the presence of low energy peaks in the source itself. Also, the radioactive source was placed in a lead collimating box which reduces stray scattering from adjacent structures and the impact of low-energetic X-rays from the source was minimized by the use of an Aluminum filter placed between the source and the detector.

Electron-hole pair formation energy W_{\pm} was measured for a wide range of electric field from 2 V/ μm to 15 V/ μm . The lower limit of applied field was determined by the ability to resolve the signal in comparison with electronic noise background, whereas the upper limit was determined by the influence of dark current. The experimental apparatus was calibrated with a Si PIN photodiode model 7787-20032-1. The value of W_{\pm} for Si =3.62 eV was assumed for the photodiode [10]. The signal generator HP model 8111A was used for estimation of system noise, consisting of preamplifier noise and the additional shot noise intrinsic in the dark current of the detector.

3.5.2.2: Results

A pulse height spectrum for $E= 14 \text{ V}/\mu\text{m}$ and photon energy $\epsilon=59.5 \text{ keV}$ is shown in Figure 3.13, where a Gaussian fit is superimposed with the background noise. For the spectral peak shown the mean value S and the spectrum width σ_{total} were determined by curve fitting. The measurements of the spectral mean values S were performed for different voltages and were found to change with applied bias as shown in Figure 3.14. The plot indicates a gradual increase in S with increase of bias. The data points were connected for better visualization of presented results.

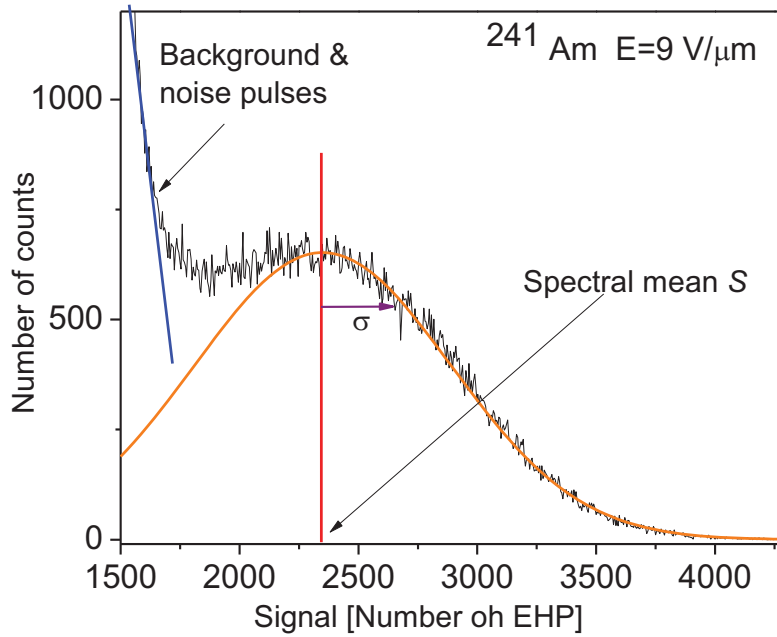


Figure 3.13: Gaussian fit of a pulse height spectrum of the $42\ \mu\text{m}$ specimen for $E=9$ V/ μm and $\epsilon=59.5$ keV are shown

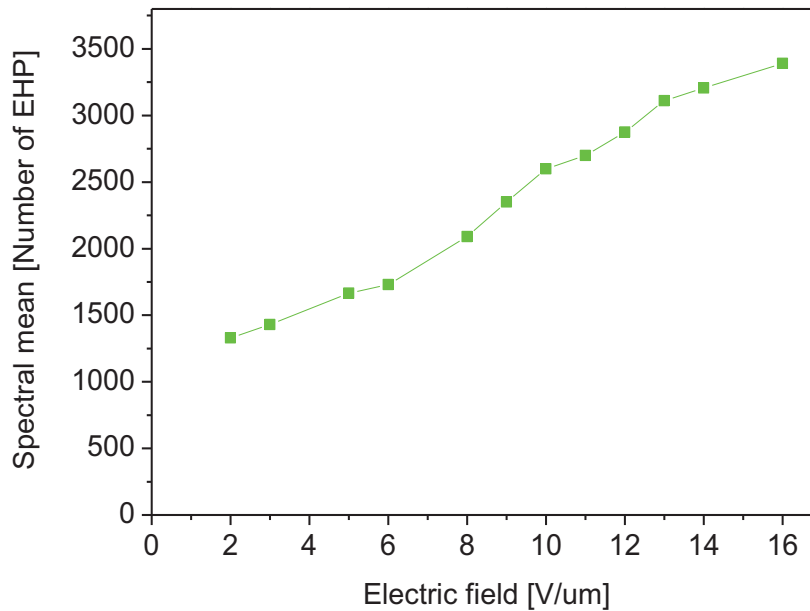


Figure 3.14: Dependence of spectral mean S on applied field is shown. The spectral mean value increases with electric field.

Knowing the spectral mean value and the energy of the incident X-ray photon, the ionization energy W_{\pm} can be found according to relation:

$$W_{\pm} = \varepsilon / S \quad (3.8)$$

Figure 3.15 shows the calculated values of W_{\pm} and its dependence on the applied field. The ionization energy W_{\pm} is seen to decrease almost linearly with electric fields up to $10\text{V}/\mu\text{m}$ and less than linearly above $10\text{V}/\mu\text{m}$. Within the range of investigated fields we did not see a saturation point for W_{\pm} and the theoretical value of W_{\pm} was also not achieved.

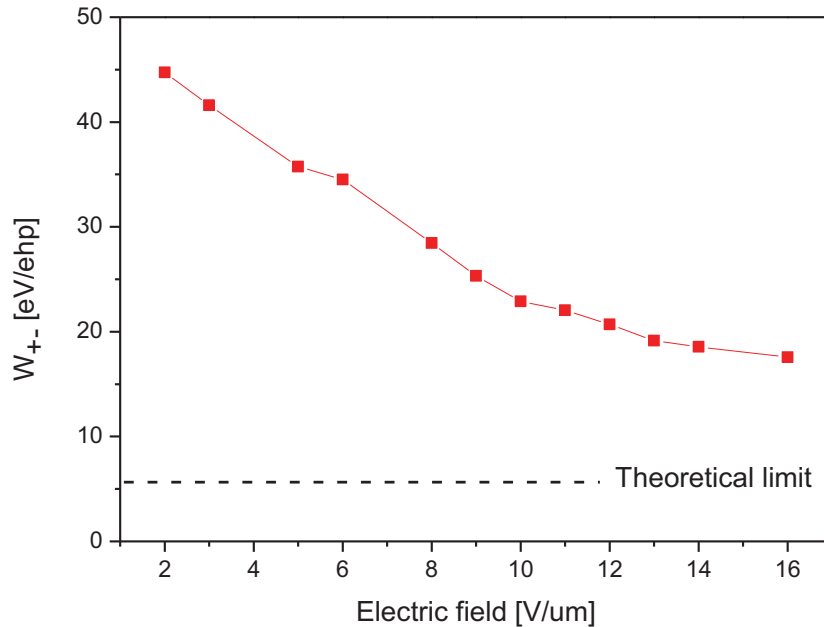


Figure 3.15: Computed values of W_{\pm} are plotted as a function of applied electric field.

3.5.2.3: Discussion: PHS noise analysis

A noise analysis was performed in order to explain the measured spectral width. It is possible to define five main components of noise limiting the total resolution of the system. They are: quantum noise of lead oxide, pulse pile-up, electronic noise, shot noise of the detector and variations in the ballistic deficit. The last four arise due to flaws in the

pulse processing system and can be greatly minimized or completely eliminated. However, the first and the most important one arise from the nature detection process, i.e. the mechanism of energy transfer of ionizing radiation to the PbO and therefore this is the fundamental noise of PbO that cannot be suppressed. These five noise components introduce their contribution to the width of the pulse heights by means of standard deviations σ_{PbO} , σ_{amp} , σ_{shot} , $\sigma_{pile-up}$ and $\sigma_{ballistic}$ respectively. Since the five processes are statistically independent, the overall standard deviation, σ_{total} , when all five are included is given by:

$$\sigma = \sqrt{\sigma_{PbO}^2 + \sigma_{amp}^2 + \sigma_{shot}^2 + \sigma_{pile-up}^2 + \sigma_{ballistic}^2} \quad (3.9)$$

If each of the five processes alone may be regarded as giving Gaussian (i.e. normal) distributions of pulse height then the resultant distribution and full width at half maximum space (FWHM) may be deduced according to the following relation:

$$\frac{S_{FWHM}}{S} = 2.36 \frac{\sigma}{N} \quad (3.10)$$

where S is the spectral mean, S_{FWHM} is the FWHM, σ is the standard deviation and N is the mean pulse height. The optimum pulse processing system would be one which reduces $\sigma_{amp}^2 + \sigma_{shot}^2 + \sigma_{pile-up}^2 + \sigma_{ballistic}^2$ to a minimum. The components of the pulse processing system such as preamplifier and mean pulse rate will govern relative magnitudes of the different noise components. The nature of the noise parameters due to detection statistics, pile up, electronic noise and ballistic deficit is discussed further both qualitatively and quantitatively.

3.5.2.3.1: Quantum noise

Quantum noise is represented by the fluctuations of the number of the charge carriers n generated by the incident X-ray photon. If the charge photogeneration process obeys the Poisson distribution, where creation of EHP is independent of creation of other pairs and characterized by some constant probability then the standard deviation is given by $\sigma = \sqrt{\bar{n}}$, where \bar{n} is the mean number of EHPs generated per incident X-ray.

However, the standard deviation is frequently different from this value and is generally expressed as:

$$\sigma_{pbo} = F\sqrt{n} \quad (3.11)$$

where F is called the Fano factor [37]. Remarkably in some materials it can be significantly less than unity.

3.5.2.3.2: Signal Pile-up

Owing to the random nature of the nuclear events there is always some probability that two events may occur so close together that they cannot be distinguished. Since the output pulses of the processing system have a finite duration there is a possibility that two such pulses will be superimposed (i.e. *pile up*) so that the pulse height analyzer will be unable to separate them and will therefore lead to an erroneous value. To minimize pile up the output pulse should be as short as possible and return to a baseline before the occurrence of another pulse. The activity of the source we used was relatively low (100 μCi), that resulted in relatively low detection rate of X-ray photons (about 5-10 pulses per second). Therefore, even with 20 μs shaping time the influence of the pile-up effect on our system can be ignored.

3.5.2.3.3: Electronic Noise from preamplifier

The main sources of electronic noise were found to be the noise of amplifier and the shot noise associated with the dark current of the detector. The electronic noise generated by the preamplifier and all subsequent processing stages is superimposed on the signal and changes the detected pulse height (increase or decrease, depending on the value of noise at detection time). As noise voltage is characterized by its standard deviation (root mean square voltage) and has mean value of zero, the mean value of the pulse height will not be affected; however it will introduce broadening of the spectrum characterized by standard deviation σ_{amp} equal to the root mean square noise voltage. The object of the pulse processing system is to reduce electronic noise as much as possible. The noise of amplifier was measured by external pulse generator and was found to be 400 e^- for 20 μs shaping time.

3.5.2.3.4: Shot noise

In the absence of radiation, pure shot noise results from the fluctuations in the number of carriers available for conduction which are assumed to behave independently. For semiconductors, the number of thermally activated carriers is usually controlled by injection currents rather than by trapping and recombination when operated in the reverse biased *PN-junction* mode. As a result the spectral noise density $\overline{i^2}$ may be written according to the relation:

$$d\overline{i^2} = \frac{e^- I_{dark}}{\pi} d\omega \quad (3.12)$$

where e^- is the elementary charge, I_{dark} is the dark current and $2\pi\omega$ is the frequency. By integrating the expression above with respect to frequency, the total shot noise can be calculated according to the relation:

$$\sigma_{shot} = \sqrt{2e^- I_{dark} B} \quad (3.13)$$

where B is the bandwidth of the amplifier through which the fluctuating signal is measured

3.5.2.4.5: Ballistic deficit

The ballistic deficit is the measure of the efficiency of the pulse processing system in terms of integration time. This problem arises when the integration time (which is related to the shaping time) is set to be less than the time needed for total charge collection generated by the detected gamma-photon. As a result only a fraction of photogenerated charge is collected within the chosen time window, and the remaining charge is lost. This shifts the position of the peak location down to the lower charge yield side. From the response to a 70 ns X-ray pulse we know the approximate time needed for all or most of the charge to be collected.

In order to check for ballistic deficit, the PHS measurement for a selected field 10 V/ μm was performed for different shaping times. Figure 3.16 shows that essentially the same charge is collected for integration times in the range 2-20 μs . The total collected

charge is found not to change significantly and does not increase with increase of shaping time indicating that the shaping time used is adequate. The scatter of spectral mean values for different shaping times is determined by the accuracy of our measurement apparatus. The choice of shaping time was therefore dictated not by ballistic deficit considerations but rather a decrease in system noise for larger integration times. Low noise of the system becomes especially important for low voltage measurements, where the spectrum peak position becomes mixed with noise. For this reason all measurements were performed with 20 μs shaping time which provided low noise and ensured complete charge collection.

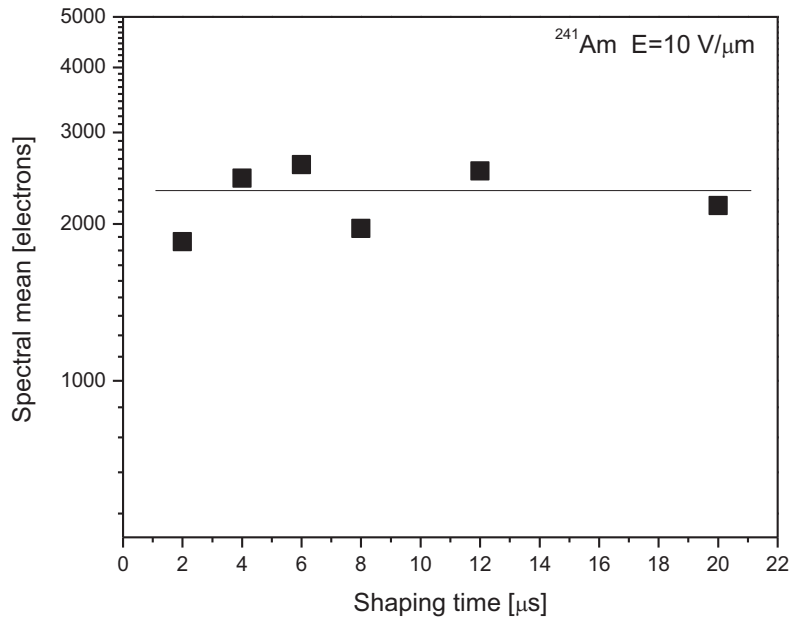


Figure 3.16: The variation of fitted peak parameter S as a function of shaping time. Uncertainties are smaller than the size of plotted points.

The effect of pulse pile-up was minimized with the use of weak radioactive source. So, the total noise of the system may be assumed to consist of the intrinsic noise of PbO, electronic noise of amplifier and dark current shot noise, so the equation 3.9 and can be simplified to the following relation:

$$\sigma_{total} = \sqrt{\sigma_{PbO}^2 + \sigma_{amp}^2 + \sigma_{shot}^2} \quad (3.14)$$

where σ_{PbO} is the fundamental noise of PbO, σ_{amp} is the electronic noise of amplifier, σ_{shot} is the shot noise of dark current. The total noise was calculated from measuring the FWHM of the spectrum taken with PbO detector. The noise of amplifier can be found by means of measuring pulse width of the signal produced by the test generator, whereas the shot noise of the dark current is relatively hard to separate from the noise of PbO as the latter is unknown. So in general it is only possible to separate the amplifier noise from the total noise. The expression above can then be rewritten as:

$$\sigma_{total} = \sqrt{\sigma_{amp}^2 + \sigma_{detector}^2} \quad (3.15)$$

where $\sigma_{detector} = \sqrt{\sigma_{PbO}^2 + \sigma_{shot}^2}$ is the detector noise due to both detection count statistics and dark current of lead oxide. Although, it is hard to measure the shot noise experimentally, the contribution of the dark current to the total noise of the system can be theoretically predicted according to the formula 3.13. Figure 3.17 shows the total system noise, detector noise, calculated quantum noise and the theoretically predicted noise of the dark current for the known bandwidth of our amplifier. As seen from the graph, the theoretical curve almost follows the measured values, meaning that the fundamental noise of the detector is low in comparison to the currently achieved dark current. The calculated quantum noise of PbO for $F=1$ (see equation 3.11) is higher than the detector noise, which suggests that Fano factor F in PbO is less than unity. This result may be verified as blocking structures will be developed, leading to a decrease in dark current and a better ability to separate the contribution of the detector statistics.

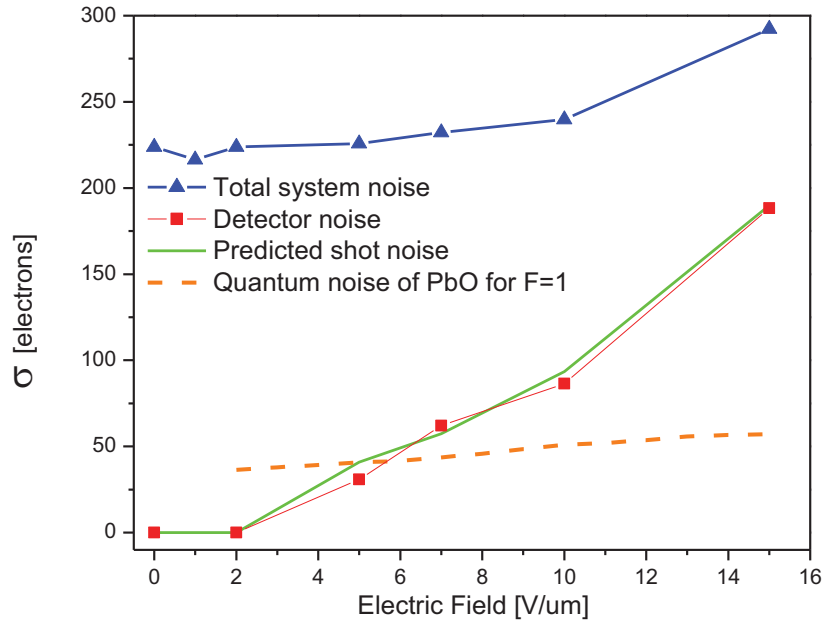


Figure 3.17: Total noise of the system, detector noise of PbO and theoretically predicted noise of lead oxide are plotted as a function of field.

3.5.2.4: Conclusion

The X-ray photogeneration in lead oxide was measured utilizing X-ray photocurrent method and PHS methods. W_{\pm} measured with PHS method was found to be about twice larger (21 eV/ehp) than one obtained with 50 ms exposure (9.7 eV/ehp) and about 4 times larger in comparison with the one at 5 s radiation pulse (5.26 eV/ehp) for the same electric field 10 V/μm. Such dependence of W_{\pm} on time might indicate on the contribution of injection to our measurements as well as on presence of deep traps in PbO. The PHS method is relatively insensitive to injection current and obtained values did not change with shaping times in a range 2-20 μs. In case of long detrapping time ($\ll 50$ ms) this method might not give a true value of W_{\pm} . On the opposite hand, X-ray photoinduced method with relatively long X-ray exposure and integration time might disguise a true W_{\pm} as it is more affected by injection and requires more investigation. However, even the highest value of W_{\pm} obtained with PHS method in PbO is about twice lower in comparison to one obtained in the same way with a-Se (45 eV/ehp). Once blocking

structure is developed, PbO might be perfect candidate for X-ray medical imaging applications.

3.6 Dark current kinetics

The measurement of dark current kinetics has been shown to be a very useful tool for material characterization [26] and, therefore, was utilized for the characterization of our PbO layers. During the experiment, an external electric field was applied to the PbO structure, while the sample was kept in complete darkness. The measurements were performed as a function of time for several different bias voltages. A computer controlled power supply (Stanford Research PS350) was utilized to create a potential difference across the sample and a programmable electrometer (Keithley 35617EBS) was used to measure the dark current. The dark current readings were taken every second for 6 hours at each constant bias. Before making the measurement at a new bias, the PbO sample was left to rest for 6 hours in complete darkness without applied electric field.

3.6.1 Analysis of the dark current decay

As shown in Figure 3.18 for the given voltages the dark current decays by about a factor of three from the initial value and saturates at a relatively low level which is comparable to the dark current level observed on the Plumbicon tubes with electron-beam read out [49]. With a positive voltage applied to the ITO electrode the dark current reaches relatively low values even without a blocking structure and the injection current is governed only by the barriers on the metal-semiconductor interface. However, an application of a modest negative field on ITO ($E = -1 \text{ V}/\mu\text{m}$) results in huge enhancement of the dark current ($I_{dark} = 200 \text{ pA}/\text{mm}^2$ and rapidly increases) in comparison to opposite positive bias applied ($\sim 10 \text{ pA}/\text{mm}^2$ see Figure 3.18). Such behavior indicates that the PbO sample with the top metal electrode behaves as a diode which is similar to what was observed in the PbO used in Plumbicon tubes. Maintaining the dark current at the lowest possible level is necessary in order to prevent the shot noise limiting the dynamic performance of the detector [38]. The exact mechanism of dark current decay in PbO shown in Figure 3.18 is not understood and thus we are

investigating it here by comparison with theories developed for other materials (a-Se, a-Si:H).

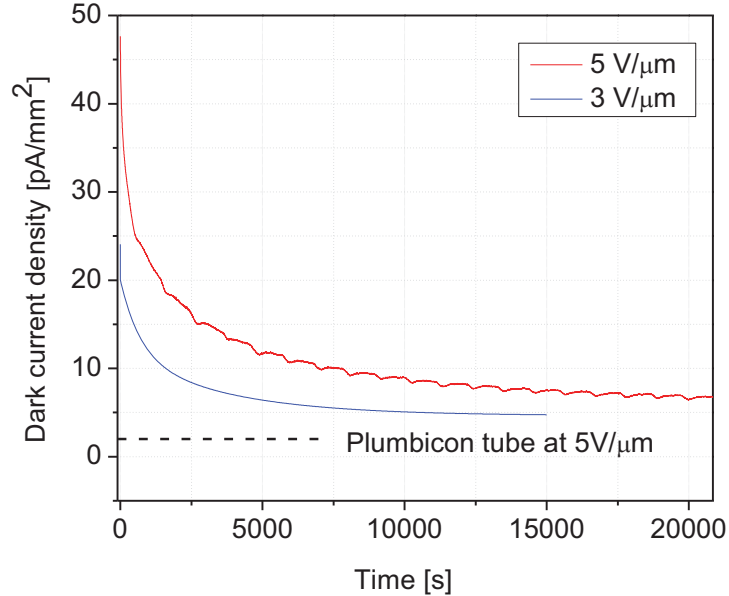


Figure 3.18: Comparison of dark current density obtained on PbO structure with metal electrodes (blue and red graphs) and electron beam readout (dashed line)

Mahmood and Kabir observed similar dark current decay with time in amorphous selenium (a-Se) multilayer $n-i-p$ structures [39]. The dark current decay was explained by carrier trapping within the n - and p - layers. These regions are relatively thin (few μm) in comparison with the thickness of i - layer. The related charge accumulation in n - and p - regions induced screening of the electric field at the metal/ n - and p -/metal layer interfaces. The resulting reduction of the electric field at the contact suppresses the carrier injection from contacts and significantly reduces the dark current which is mainly controlled by the injection.

An alternative model that explains the dark current decay in hydrogenated amorphous silicon (a-Si:H) $p-i-n$ structures was suggested by Street [40, 41]. He explains the decay of dark current with time by depletion of charge from the bulk of i -layer assuming that the dark current is controlled by thermal generation from defect states in the gap. As

traps are depleting, the quasi Fermi level moves toward the midgap and the thermal generation current decreases [40]. The model developed by Street is more applicable in our case, because due to the polycrystalline nature of PbO the distribution of defects across the sample thickness can be assumed to be uniform. This results in a uniform distribution of electric field across the sample (neglecting the thin contact interface regions).

For better understanding of dark current kinetics observed in our PbO layers we first considered intrinsic properties of α -PbO, as it is the major constituent of grown films. For such analysis we have used the data on carrier effective masses established elsewhere [43], in which the hole effective mass (for in-plane directions $m_{\parallel}^* = 5.91 m_0$ and for out-of-plane $m_{\perp}^* = 1.12 m_0$) was found to be much heavier than the effective mass of electrons ($m_{\parallel}^* = 0.41 m_0, m_{\perp}^* = 0.47 m_0$). Based on carrier effective masses, the effective density of states has been calculated for the electrons in conduction band to be $N_C = 7.15 * 10^{18} \text{ cm}^{-3}$ and for the holes N_V in the valence band $N_V = 1.58 * 10^{18} \text{ cm}^{-3}$ and the intrinsic carrier density is found to be $n_i = 4.45 * 10^3 \text{ cm}^{-3}$ [45]. The difference in the effective density of states for electrons and holes results in the shift of Fermi level from midgap towards the conduction band on 0.04 eV and induces the n -type nature of α -PbO even in the absence of impurities.

However, according to Ref. [29] the defects in the crystal lattice might be also responsible for pinning of the Fermi level somewhat closer to the conduction band. PbO has a layered structure, composed of *platelets* or *crystallites* that can be considered as single crystals where the depletion zone induced by the surface states extends over whole crystallite [29]. Taking into account that the most feasible source of the defects in thermally evaporated oxides is known to be the oxygen vacancies appearing due to the oxygen deficiency [34], we can assign the surface states at the crystallite boundaries to this particular type of defect. We anticipate that the generation of the defect states on the surface of each platelet is characterized by the same probability regardless of whether the platelet is located at semiconductor/metal interface or in the bulk of the material. The concentration of these defects is expected to be quite high in the sample (experimentally

predicted value is $\sim 10^{13} \text{ cm}^{-2}$ [29]) as their formation energy is relatively low (theoretically estimated formation energy is 3.13 eV [43]).

In [43] it was shown that the oxygen vacancies (V^0) induce the deep strongly localized defect level within the band gap located at $E_D(V^0) = 1.03 \text{ eV}$ above the top of the valence band E_V i.e. above the midgap as the size of bandgap $E_g = 1.9 \text{ eV}$ [29]. The formation energy of the lead vacancies (6.32 eV [43]) is almost twice larger than that for oxygen vacancies (3.13 eV [43]), so its concentration is expected to be much lower than that of the oxygen vacancy. The oxygen vacancy is found to have three charged states $q(0, 1+, 2+)$. In its uncharged state $q=0$ ($V^{0(0)}$ state) the oxygen vacancy is already occupied by two electrons. If the oxygen vacancy could release one or two electrons it would appear in $1+$ ($V^{0(1+)}$) or $2+$ ($V^{0(2+)}$) charged states, respectively. The oxygen vacancies in a charge state when one ($V^{0(1+)}$) or two electrons ($V^{0(0)}$) occupy the vacancy site would act as n -type dopant. The doping levels and therefore the position of the Fermi level would be governed by the concentration of the oxygen vacancies and particularly by the concentration of the electrons occupying them. Because the oxygen vacancies are located deep inside the band gap and their activation energy is about $E_a = 0.87 \text{ eV}$ (calculated as $E_g - E_D(V^0)$), the thermally generated release of the trapped charge would be quite slow as it depends exponentially on the inverse of the activation energy $\sim \omega^{-1} e^{-(E_a)/k_B T}$, where $\omega \sim 10^{13} \text{ s}^{-1}$ is the excitation rate factor. The external field could then initiate the release of the carriers from the traps and this process would be observed at the dark current kinetics. Thus, we believe that a possible mechanism contributing to dark current kinetics is the bias-induced release of electrons originally occupying the oxygen defects.

In Figure 3.19 we have plotted the dark current decay for different negative biases applied to the top Au contact. The dark current shows an initial decay after voltage is applied and its relaxation time to the steady state I_{st} is by the time constant $\tau_{st} = 1.5 * 10^4 \text{ s}$. The value of I_{st} is defined by the injection from the contacts when the depletion process is complete. Therefore I_{st} depends on the applied bias and it is almost doubled as bias increases from 3 to 7 V/ μm .

From the current kinetics we calculated the depletion charge Q_d as indicated by the shaded region in Figure 3.23, where I_{st} is the value of the steady state current when charge depletion is balanced by the injection current at $\tau_{st} = 1.5 * 10^4$ s (about half of the total charge depletion occurs during the first 3000 sec).

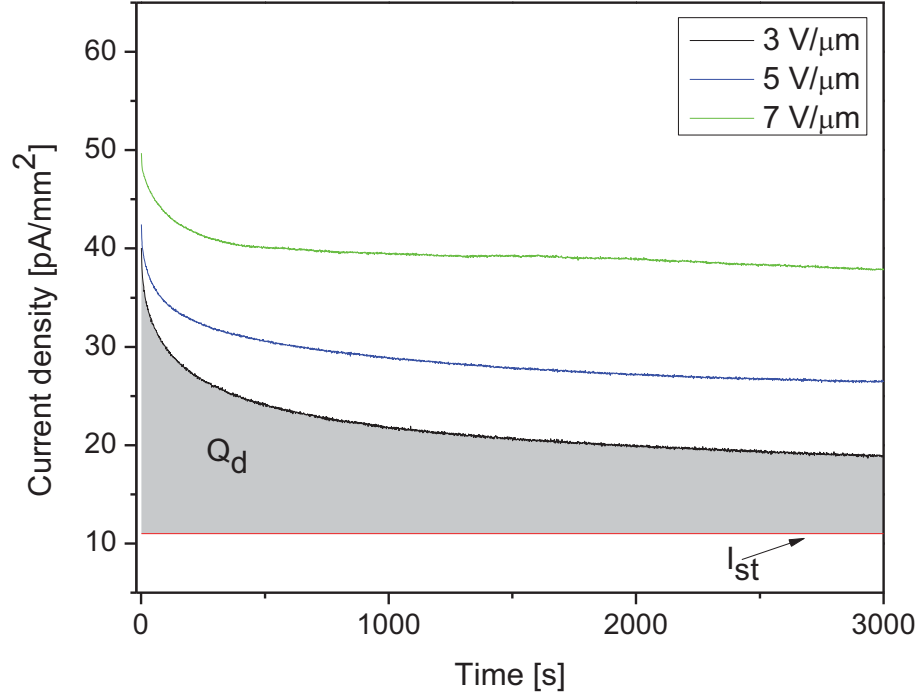


Figure 3.19: Figure shows the kinetics of the dark current at the different bias: where I_{st} indicates the level of steady state dark current and Q_d is the the total depleted charge.

The density of states accounting for the electrons localized on the oxygen vacancies can be defined from the depletion process as:

$$N_D = \frac{Q_D}{e^{-}L} \approx 4.45 * 10^{15} \text{ cm}^{-3} \quad (3.16)$$

where e^{-} is elementary charge and L is the thickness of the PbO sample (42 μm). The density of states obtained for these measurements ($N_D L = 1.9 * 10^{13} \text{ cm}^{-2}$) is in reasonable agreement with the previously experimentally estimated density of states ($\sim 10^{13} \text{ cm}^{-2}$) reported elsewhere [29].

3.5.3.2: Results and discussion

Upon depletion of the traps, the quasi-Fermi level E_{FD} which defines the occupancy of the localized states shifts towards the intrinsic Fermi level position ($E_{Fi} = 0.04 \text{ eV} + 1/2E_G$). Therefore, the position of the Fermi level varies with the doping densities N_D and we can find the location of the quasi-Fermi level for n -type semiconductor from the relation [45]:

$$E_{FD} - E_{Fi} = k_B T \ln(N_D/n_i) \quad (3.17)$$

where k_B is the Boltzmann constant and T is the temperature ($T=300 \text{ K}$), h is Planck's constant, n_i is the intrinsic carrier density of pure α -PbO (without vacancies). For the value of N_D that was earlier defined from the dark current kinetics we estimate the shift of the quasi-Fermi level to be $E_{FD} - E_{Fi} = 0.72 \text{ eV}$, provided that full depletion and complete charge collection occurs within $\tau_{st} = 1.5 * 10^4 \text{ s}$. The shift of the Fermi level causes a modification of the potential profile at the interface metal/semiconductor and thus governs the carrier injection from the contacts. Based on comparison of the work functions of Au, PbO and ITO materials utilized in our system ($q\chi_{Au} = 5.1 \text{ eV}$ [47], $q\chi_{PbO} = 4.85 \text{ eV}$ for the Fermi level located in the midgap [48], $q\chi_{ITO} = 4.3 \text{ eV}$ [46]), we found that the potential barrier for injection of electrons from the Au contact is lower by 0.3 eV than that for holes injected from the ITO contact as shown in Figure 3.20 below.

Taking into account that the hole potential barrier grows with the shift of E_{FD} towards the conduction band, we can neglect the contribution to I_{st} of the hole injection from the ITO contact and consider only injection of electrons from the Au contact. The alteration of the potential profile at the Au/PbO interface with charge depletion is shown in Figure 3.21.

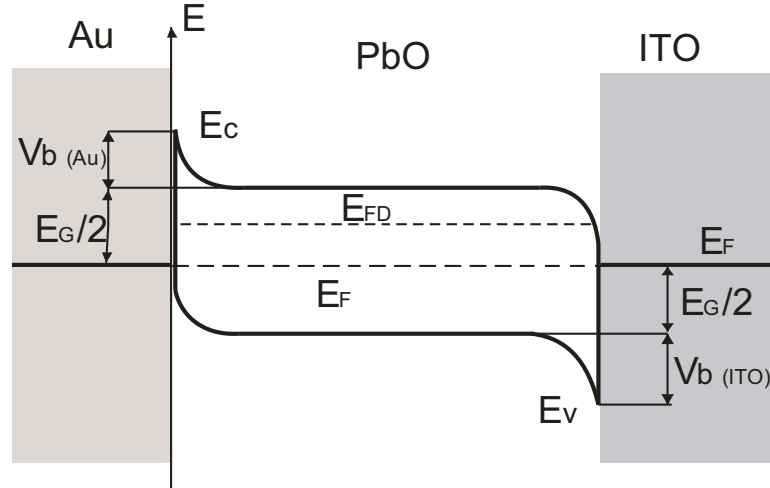


Figure 3.20: The energy diagram of the Au/PbO/ITO system. The $V_{b(Au)}$ and the $V_{b(ITO)}$ are the difference of the work functions at the interfaces Au/PbO and PbO/ITO respectively.

In the instant after the electric field is applied $t_0 = 0$ s (Figure 3.21 a) the localized states have their maximum occupancy and the quasi-Fermi level E_{FD} is elevated the conduction band by 0.72 eV from its intrinsic position and the potential barrier for electrons being injected from the Au electrode is $U_{initial}^e = V_0 \sim 0.5$ eV. With time the localized states become depopulated while results in the increase of the potential barrier for electrons as the Fermi level is shifted down. In case of full depletion the barrier reaches its maximal height $U_{final}^e = 0.5\text{eV} + (E_{FD} - E_{Fi})$ (Figure 3.21 b).

The process of charge release from traps is thermo-generated. In order to investigate this process more deeply the computer controlled LINKAM system was used to obtain the dark current kinetics at both high and low temperature. Figure 3.22 show the temperature dependence of the dark current for the same bias (3 V/ μm). The level of dark current is seen to depend strongly on the temperature, indicating a major contribution of thermally generated charge carriers to the measured current. As expected, the relaxation time of the depletion process was found to decrease with both increasing the temperature and applied electric field due more efficient release of electrons from the oxygen vacancies.

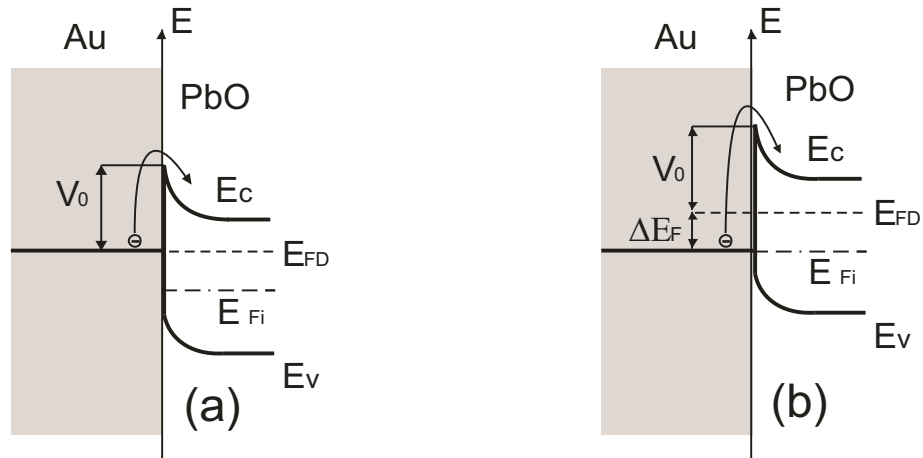


Figure 3.21: The scheme shows the modification of the potential barrier at the Au/PbO interface. As oxygen defects release their electrons the quasi-Fermi level E_{FD} shifts towards the intrinsic E_{Fi} value. a) The profile of potential barrier when external field is applied ($t_0 = 0$). b) The potential profile for the final state at $\tau_{st} = 1.5 \cdot 10^4$ s .

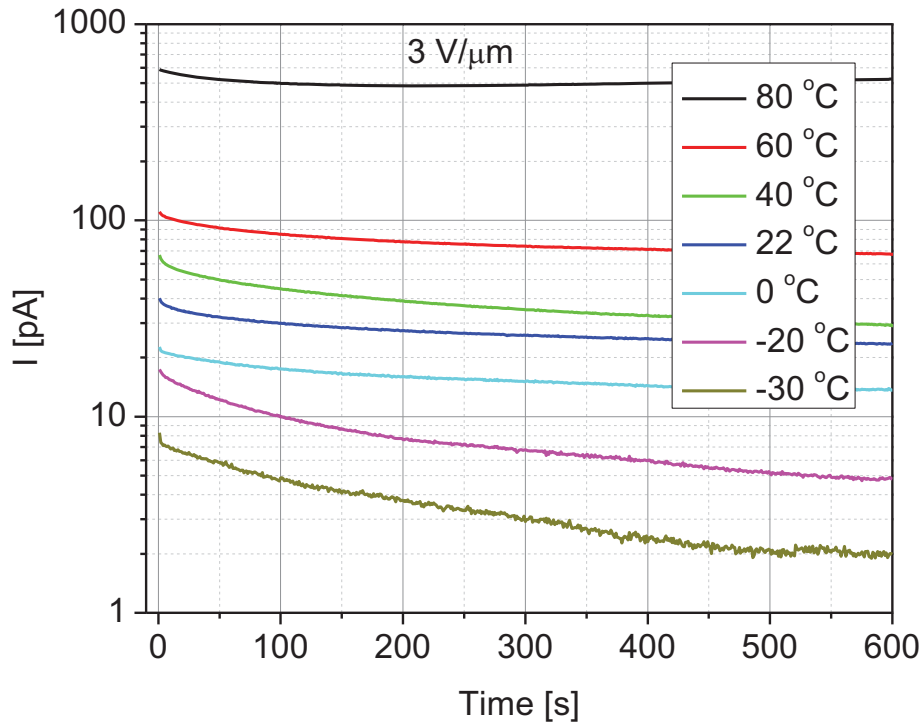


Figure 3.22: The temperature dependence of the dark current kinetics is shown for a range of temperatures above and below room temperature.

3.5.3.3: Conclusion

Based on analysis of the dark current kinetics we found that transport processes in the PbO layers are controlled by a high concentration of oxygen vacancy defects. Oxygen vacancies act as deep traps for electrons affecting the temporal behavior of the dark current. Secondly, electrons localized on the vacancy site induce the *n*-type doping thereby shifting the Fermi level from its intrinsic value closer to the conduction band by 0.72 eV.

The observed decay of the thermally generated current is governed by two main processes: depletion of the charge from oxygen vacancies and as depletion process is completed the dark current is controlled by injection of electrons from the Au contact. The relaxation time of the depletion process is found to be $\tau_{st} = 1.5 * 10^4$ s at $T=300$ K. This relaxation time was found to become shorter with temperature increase and applied field. This is due to the fact that release of the electrons from the oxygen vacancies becomes more efficient.

To summarize, the results presented here provide an insight into the nature of defects in PbO clarifying their electronic and charge states and explaining why vacancies exist in high concentration in thermally evaporated PbO layers. Moreover, our own experimental results on time dependence of the dark current density suggest that it is the field dependent occupancy of oxygen vacancies that governs the dark current kinetics. Since oxygen vacancies play an essential role in the transport properties of PbO layers, material science solutions must be found to improve PbO layers deposition techniques in order to suppress their appearance. Methods to consider include thermal evaporation, optional low energy oxygen ion bombardment or passivation of vacancies by post-growth annealing in oxygen atmosphere as well as the development of a blocking structure that will suppress injection from the contacts and maintain dark current at low level.

Chapter 4: Future work

4.1: Summary of the thesis

The properties of lead oxide (PbO), a novel photoconductor for direct X-ray-to charge application for application in medical imaging were investigated in this work. The samples of PbO were produced with a deposition technique that allowed us to obtain an improved layer composition. The improvement was established in terms of a high fraction of α -PbO and low fraction of β -PbO. The composition of the deposited films governs their electro-optical and radiation response properties, so a number of experiments were performed to characterize the material. They include the analysis of the temporal response of PbO to X-rays, its charge yield and the dark current.

The data obtained from the PbO response to a short (70 ns) X-ray pulse performed at different temperatures and for a wide range of electric fields showed a relatively fast response for lead oxide. However, the mobility of the fast carriers (electrons) was found to be at least five times higher than for holes and $\sim 1.4 \text{ cm}^2/\text{Vs}$. For the 42 μm PbO sample at bias of 3 $\text{V}/\mu\text{m}$ the majority of created charge was collected during the first 500 ns. Fast transit time of carriers and low trapping (or fast release of trapped carriers) is needed in order to ensure that during the read out time all charge will be collected and there is no carryover of image charge generated by previous X-ray exposure into subsequent image frames (Lag). High charge yield (low electron-hole pair formation energy) is needed for high signal-to-noise ratio (SNR) of the detector which determines the image quality. Improved SNR is a very important parameter of the detector as it permits either a decrease the radiation dose to the patient without degrading the image quality or alternatively an improved image quality with the same dose.

The experiments on the charge yield were performed with both the X-ray induced photocurrent and the PHS methods. The experiments showed good charge yield, higher (almost by factor of 2 at 10 $\text{V}/\mu\text{m}$) than in a-Se – the only commercially available direct conversion X-ray imaging detector. Although, the theoretical limit of charge yield was not achieved in these experiments it was shown to increase with increase of applied field.

The values of W_{\pm} obtained by PHS method for same voltage did not change significantly with shaping time in the range 2-20 μ s. However, W_{\pm} was shown to increase with increase in X-ray pulse duration. This might indicate a charge injection from the bias electrodes and/or a release of charge carriers from the deep traps and requires further investigation.

Another parameter that governs the dynamic performance of the detector is the shot noise intrinsic to the dark current of detector. The dark current of PbO with metal electrodes was seen to decay with time to a level comparable with the dark current levels previously observed on the Plumbicon vacuum video tubes with electron beam read out. The kinetics of the dark current was analyzed both quantitatively and qualitatively. Such behavior was found to be governed by charge depletion from the oxygen vacancy defects under constant bias. However, the magnitude of the current decays with time as the quasi-Fermi level shifts closer to the midband i.e., the potential barrier for electrons to be injected grows. The contribution of hole injection from the ITO contact was found to be negligible as the potential barrier for holes is higher than for electrons. A deficiency of oxygen during the deposition process is assumed to be the reason for the oxygen vacancies.

4.2: PbO blocking structure

We suggest that thermal vacuum evaporation of PbO with low energy oxygen ion bombardment or in a small partial pressure of H₂O gas in order to minimize the appearance of oxygen vacancies. This technique may also improve the composition of the PbO layer, i.e. increase the fraction of α -PbO in the grown films. Another possible improvement is the post-growth annealing in an oxygen gas. The annealing of PbO even at relatively low temperatures (within the tolerance of amorphous silicon TFT arrays) was shown to increase X-ray charge yield and decrease dark current. Our previous approaches were oriented towards the improvement of the PbO performance by improving the morphology of the grown layer, however, a maximum dark current limit on the order of 10 pA/mm² is required for practical AMFPI operation [22]. Recent experiments on other detectors have shown that this low dark current typically can only be achieved in a

multilayer detector [38], where blocking structures were incorporated at the semiconductor-electrode interfaces. The PbO blocking structure must be developed as a part of future work that would allow application of high electric fields (to increase W_{\pm}) while maintaining low levels of the dark current. The proposed method is to develop blocking contacts that would be heavily doped with localized trapping centers for holes at the positive electrode (*P-layer*), thereby preventing hole injection while permitting electron transport (see Figure 4.1). The *N-layer* at the negative electrode would be analogous, but with signs reversed. Then upon first application of the bias potential, charge carriers are injected from the conducting electrodes into the blocking contacts, where they are trapped. This injection process is self-regulating in that the trapped charges in the blocking contacts will reduce the field across the PbO–electrode interfaces, thereby preventing further injection of dark carriers.

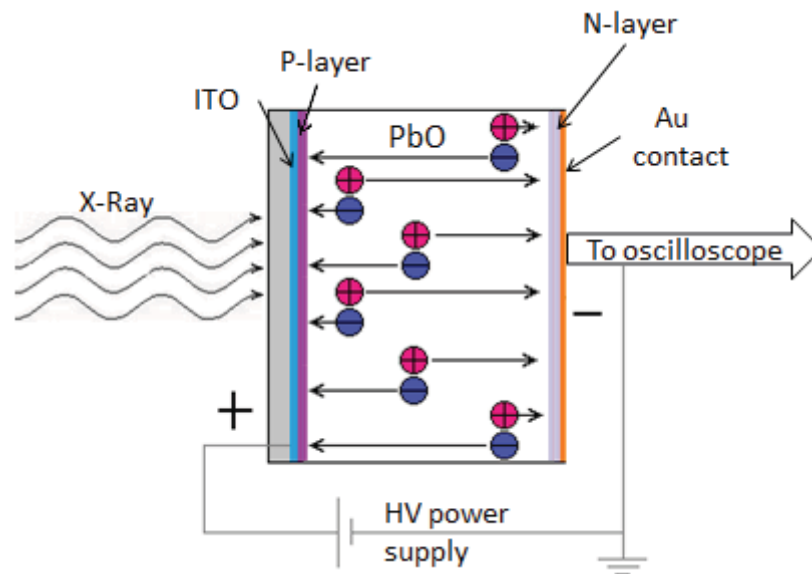


Figure 4.1: PbO blocking structure is shown. The additional layers of blocking contacts suppress charge injection inside the sample, while allowing the charge to come out freely from the sample.

Currently, at all times the PbO samples are kept under a constant flow of dry nitrogen gas. This provides a neutral environment around the sample and protects it from atmospheric degradation as a result of interaction of PbO with CO_2 and H_2O molecules. This is not suitable for a practical detector, so another function of the blocking contact at

the Au side would be to serve as a protection from the impact of the environment thereby keeping the properties of the photoconductive PbO layers from degrading.

Bibliography

- 1) T. S. Curry, J. E. Dowdey and R. C. Murry, Jr, “Christensen’s Physics of Diagnostic Radiology”, Lea and Febiger (1990).
- 2) H. E. Johns, J. R. Cunningham, “The Physics of Radiology”, American Lecture series (1977).
- 3) S. R. Cherry, J. A. Sorenson and M. E. Phelps, “Physics in Nuclear Medicine”, Saunders (2003).
- 4) J. Beutel, H. L. Kundel and R. L. Van Metter, “Handbook of Medical Imaging”, SPIE Press (2000).
- 5) J. A. Seibert, J. M. Boone, “X-Ray Physics for Nuclear Medicine Technologists. Part 2: X-Ray Interactions and Image Formation”, Journal of Nuclear Medicine Technology 33:3-18 (2005).
- 6) G. Zentai, “Photoconductor-based (direct) large-area x-ray imagers”, DOI#10.1889/JSID 17.6.543.
- 7) J. A. Seibert, “Flat-panel detectors: how much better are they?” Springer (2006).
- 8) R. D. MacDougall, I. Koprinarov, J. A. Rowlands, “The x-ray light valve: A low cost, digital radiographic imaging systems – Spatial resolution”, American Association of Physicists in Medicine (2008).
- 9) A. Brauers, G. Frings, U. Schiebel, “Do and don’t in the growth of PbO layers for a flat dynamic X-ray detector”, PFL Aachen Report No. 1194/96 (1996).
- 10) L.D. Madsen and L. Weaver, “Characterization of Lead Oxide Thin Films Produced by CVD”, J. Am. Ceram. Soc. 81(4), 988 (1998).
- 11) Y. Pauleau and E. Harry, “Reactive sputter-deposition and characterization of lead oxide films”, J. Vac. Sci. Technol. A 14(4), 2207 (1996).
- 12) M. Baleva and V. Tuncheva, “Optical Characterization of Lead Monoxide Films Grown by Laser-Assisted Deposition”, Journal of Solid State Chemistry 110, 36 (1994).
- 13) M. Simon, “Lead Oxide for Direct Conversion FDXD. New Measurements”, PFL Aachen Report 1509/2001 (2001).

- 14) A. v.d. Drift, "Texture of a vapor-deposited lead-monoxide layer", Philips Res. Rep. 21, 289 (1966).
- 15) M. Baleva, V. Tuncheva, J. Solid State Chemistry, Vol. 110 (1994) 36-42
- 16) H. J. Terpstra, R. A. de Groot, C. Haas, "Electronic structure of lead monoxides: Band-structure calculations and photoelectron spectra", Physical Review B 52 (16) 11691 (1995)
- 17) D. U. Wiechert, S. P. Grabowski, M. Simon, "Raman spectroscopic investigation of evaporated PbO layers", Elsevier (2005).
- 18) D. U. Wiechert, S. P. Grabowski, M. Simon, "Raman Spectroscopic Investigation of PbO Layers", PFL Aachen Report 1678/2003 (2003).
- 19) Internet Raman spectroscopic Database:
www.chem.ucl.ac.uk/resources/raman/pigfiles/redlead.html
- 20) C. A. Webster, I. Koprinarov, S. Germann, J. A. Rowlands, "The x-ray light valve: A potentially low cost, digital radiographic imaging system-concept and implementation considerations", Med. Phys. 35 (3) 939-948 (2008).
- 21) S. Kasap, J. B. Frey, G. Belev, O. Tousignant, H. Mani, J. Greenspan, L. Laperriere, O. Bubon, A. Reznik, G. DeCrescenzo, K. S. Karim, J. A. Rowlands, "Amorphous and Polycrystalline Photoconductors for Direct Conversion Flat Panel X-Ray Image Sensors", Sensors 11 5122 (2010).
- 22) Y. L. E. Antonuk, "A-Si:H TFT-based active matrix flat-panel imagers for medical X-ray applications," in *Materials and Processes: Amorphous Silicon Thin Film Transistors*, Y. Kuo, Ed. Norwell, MA: Kluwer, 2003, vol. 1, ch. 10, pp. 395-484).
- 23) A.W. Rau, L. Bakueva and J. A. Rowlands, "The x-ray time of flight method for investigation of ghosting in amorphous selenium-based flat panel medical x-ray imagers", Medical Physics 32 (10) 3160-3177 (2005).
- 24) M. Simon, R. A. Ford, A. R. Franklin, S. P. Grabowski, B. Menser, A. Nascetti, M. Overdick, M. J. Powell, D. U. Wiechert, "Analysis of Lead Oxide (PbO) Layers for Direct Conversion X-Ray Detection", IEEE vol. 52 2037(2005).
- 25) R. A. Street, "Thermal generation currents in hydrogenated amorphous silicon p-i-n structures", Appl. Phys. Lett. 57 (13) 1334-1336 (1990).

- 26) B. Schrader “Infrared and Raman Spectroscopy”, Weinhein ISBN 3-527-26446-9
- 27) M. J. Pelletier “Analytical Applications of Raman Spectroscopy”, ISBN 0-632-05305-4.
- 28) J.J. Laserna, “Modern Techniques in Raman Spectroscopy”, John Wiley & Sons, ISBN 0-471-95774-7.
- 29) L. M. Biberman S. Nudelman “Photoelectronic imaging devices”, vol. 2, 275, Plenum press (1971).
- 30) A. Reznik, B.J.M. Lui, Y. Ohkawa, T. Matsubara, K. Miyakawa, M. Kubota, K. Tanioka, T. Kawai, W. Zhao, J.A. Rowlands, NuclInstrum Methods Phys Res A 567 93 (2006).
- 31) <http://www.asiinstr.com/technical/Dielectric%20Constants.htm>
- 32) J. van den Broek “The electrical behavior of vapor-deposited lead-monoxide layers” Philips report 22,367 (1967).
- 33) S. Kasap and P. Capper, “Springer Handbook of Electronic and Photonic Materials” (2006).
- 34) O.H Hwang, S. S. Kim, J. H. Suh, S. H. Cho and K. H. Kim, “Effect of thermal annealing of lead oxide film” Nuclear Instruments and methods in physics research A 633 70 (2011).
- 35) S. Cho, S. Kang, C. Kwon, M. S. Yun, J. Park, S. Park, J. Y. Choi, C. Mun, H. Lee and S. Nam, “Effect of annealing on the X-ray detection properties of nano-size polycrystalline lead oxide films”, Japanese Journal of Applied Physics 47 (9) 7396 (2008).
- 36) M. Blevis, D. C. Hunt, J. A. Rowlands “Measurement of X-ray photogeneration in amorphous selenium”, Journal of applied physics, 85 (11) 7958 (1999).
- 37) P. W. Nicholson “Nuclear Electronics” John Wiley (1974)
- 38) S. A. Mahmood, M. Z. Kabir, O. Tousignant, H. Mani, J. Greenspan, P. Botka “Dark current in multilayer amorphous selenium x-ray imaging detectors”, Applied Physic Letters 92, 223506-1 (2008).
- 39) S.A. Mahmood, M.Z. Kabir, J. Vac. Sci. Technol. A 29, 031603 (2011).
- 40) R. A. Street “Long-time transient conduction in a-Si:H p-i-n devices”, Philosophical Magazine B, 63 (6) 1343 (1991).

- 41) R.A. Street, S.E. Ready, F. Lemmi, K.S. Shah, P. Bennett, Y. Dmitriyev, J. Appl. Phys. 86,5 (1999).
- 42) S. Kasap, J. B. Frey, G. Belev, O. Tousignant, H. Mani, L. Laperriere, A. Reznik, J. A. Rowlands, Physical Status Solidi (b), 246, 1794 (2009).
- 43) J. Berashevich, O. Semeniuk, O. Rubel, J. A. Rowlands, A. Reznik “Lead monoxide a-PbO: electronic properties and point defect formation” submitted for review.
- 44) B. Thangaraju, P. Kaliannann, Semicond. Sci. Technol. 15, 542 (2000).
- 45) S. M. Sze, Physics of Semiconductor devices, 2-nd edition, John Wiley, (1981).
- 46) Y. Park, V. Choong, B. R. Hsieh, Y. Gao, C. W. Tang, App. Phys. Lett. 68, 2699, (1996).
- 47) J. S. Kim, B. Lagel, E. Moons, N. Johansson, I. D. Baikie, W. R. Salaneck, R. H. Friend, F. Cacialli, Synthetic Metals 111-1112, 311 (2000).
- 48) M. Simon “Electrical contacts on PbO-layers”, PFL–Aachen/Hamburg/Paris Technical Note 20 (2003).
- 49) F. J. du Chatenier, O. P. van Driel “Quantitative approach to the fabulous Plumbicons” Nat. Lab. Report# 5240
- 50) <http://whs.wsd.wednet.edu/faculty/busse/mathhomepage/busseclasses/radiationphysics/lecturenotes/chapter12>
- 51) J. A. Seibert and J. M. Boone, “X-Ray Imaging Physics for Nuclear Medicine Technologists. Part 2: X-Ray Interactions and Image Formation”, Journal of Nuclear Medicine Technology, 33:3-18 (2005).
- 52) M. Z. Kabir, “Effects of charge carrier trapping on polycrystalline PbO X-ray imaging detectors”, Journal of Applied Physics 104, 074506 (2008)